JOURNAL OF GEOPHYSICAL RESEARCH, VOL. , NO. , PAGES 1–42,

Assessment of global 3-D models based on regional ground truth locations and travel times

M.H. Ritzwoller, N.M. Shapiro, A.L. Levshin, E.A. Bergman, E.R. Engdahl

Center for Imaging the Earth's Interior, Department of Physics, University of Colorado at Boulder, Boulder, Colorado, USA

M.H. Ritzwoller, Department of Physics, University of Colorado at Boulder, Boulder, CO 80309-0390, USA. (ritzwoller@ciei.colorado.edu)

N.M. Shapiro, Department of Physics, University of Colorado at Boulder, Boulder, CO 80309-0390, USA. (nshapiro@ciei.colorado.edu)

A.L. Levshin, Department of Physics, University of Colorado at Boulder, Boulder, CO 80309-0390, USA. (levshin@ciei.colorado.edu)

E.A. Bergman, Department of Physics, University of Colorado at Boulder, Boulder, CO 80309-0390, USA. (bergmane@ciei.colorado.edu)

E.R. Engdahl, Department of Physics, University of Colorado at Boulder, Boulder, CO 80309-0390, USA. (engdahl@ciei.colorado.edu)

Abstract. We have assembled a data set of nearly 1000 events across Eurasia and North Africa whose locations and origin times are known with uncommon accuracy. These "Ground Truth" (GT) events, which occur in 23 event clusters, the groomed P and P_n arrival time data observed at regional distances ($\Delta < 20^\circ$), and about 1000 empirical phase path anomalies that are constructed from each of the clusters, create a GT data base to be used to assess the quality of 3-D models and their applicability to regional locations. We assess several seismic models of the crust and upper mantle, concentrating on the 1-D model AK135 and the 3-D v_s model CUB2.0. Two assessments are performed: (1) the fit of model predicted travel times to the empirical phase path anomalies and (2) the ability to locate the GT events. The 3-D v_p model converted from CUB2.0 v_s using the thermoelastic properties of an assumed mantle composition fits regional P and P_n travel times remarkably well, both in geographical pattern and absolute level. Rms-misfit is about 1.0 sec for explosions, and 1.25 sec and 1.55 sec for earthquakes whose locations are known to about 5 km and 10 km, respectively. We conclude on the basis of the location assessments that the intrinsic regional location accuracy is $\sim$ 5 km for the 3-D model and $\sim$ 10km for the 1-D model. As the number of stations reduce, both 1-D and 3-D model locations degrade and variance increases, but even with only 5 recording stations the 3-D model deliver better locations for about 75% of events. Our findings underscore the importance of GT data bases in assessing 3-D models, and show that global 3-D v_s models provide a sound basis on which to build improvements in regional location capabilities.

1. Introduction

The seismic location inverse problem has a history dating back almost a century, at least to *Geiger* [1912]. In recent years there has been a resurgence of interest in improving abilities to estimate reliable seismic locations (earthquakes, explosions) [e.g., *Thurber & Rabinowitz*, 2000]. There are several reasons for this. First, there is the desire to apply advances in seismological models and practice to improve the locations contained in global catalogs produced, for example, by the International Seismological Centre (ISC), the U.S. National Earthquake Information Service (NEIS), or the International Data Center (IDC) in Vienna. Second, there is greater emphasis now on small earthquake location that has been generated by the Comprehensive Nuclear Test-Ban Treaty (CTBT), which specifies a location uncertainty of 1000 km^2 or less for events with magnitudes greater than or equal to 4.0 [e.g., *Ringdal & Kennett*, 2001]. Third, there has been growing recognition of the importance of high quality locations in seismic tomography and fault zone characterization. Efforts to improve the location of seismic events have fallen into two broad categories: (1) advances in travel time models to improve absolute locations and (2) the development of multiple event location methods to improve relative location capabilities. These categories are not entirely disjoint because if a cluster of relatively located events contains one or more reference events with well-constrained absolute locations, the relatively located events can be tied to absolute locations.

Attempts to improve body wave travel time models divide into teleseismic and regional studies, where regional distances are generally defined as less than about 20°. Recent efforts to improve teleseismic location capabilities have concentrated on the application of current-generation 1-D and 3-D mantle models. For example, *Engdahl et al.* [1998]

showed that global improvements in teleseismic locations are possible by applying new methods using the 1-D model AK135 [*Kennett et al.*, 1995]. Several researchers have investigated how the use of 3-D tomographic models of the whole mantle affects hypocenter determinations based on teleseismic travel time data [e.g., *Smith & Ekström*, 1996; *Antolik et al.*, 2001; *Chen & Willemann*, 2001]. These studies have established that teleseismic mislocations are reduced relative to 1-D model locations (e.g., Jeffreys-Bullen travel-time tables [*Jeffreys & Bullen*, 1940], PREM [*Dziewonski & Anderson*, 1981], IASP91 [*Kennett & Engdahl*, 1991]) when recent generation 3-D mantle models based on either global [e.g., *Su et al.*, 1994; *Su & Dziewonski*, 1997] or local basis functions [e.g., *van der Hilst et al.*, 1997; *Bijwaard et al.*, 1998; *Boschi & Dziewonski*, 1999] are applied. Efforts to predict travel times with empirical teleseismic heterogeneity corrections have been more rare [e.g., *Piromallo & Morelli*, 2001]. At regional distances, travel time predictions depend on the ability to model the crust and upper mantle. Regional travel time predictions are less accurate than teleseismic predictions because heterogeneity is much stronger and because data that constrain the crust and upper mantle are more limited in distribution and somewhat more difficult to interpret unambiguously. In addition, regional triplication crossover distances are highly variable which makes it difficult to identify phases correctly. This is true both for P_n triplications, as well as for distinguishing P_n from P arrivals. For these reasons, model-based approaches to predicting regional travel times [e.g., *Firbas*, 2000] have played a subordinate role to the development of purely empirical corrections [e.g., *Myers & Schultz*, 2000] that are combined with spatial interpolation schemes [e.g., *Schultz et al.*, 1998].

The result, however, is that the ability of 3-D models to predict regional travel times remains largely uninvestigated and, consequently, the applicability of 3-D models to regional location exercises is poorly understood. The purpose of this paper is to fill in this gap in knowledge. We are able to take this step for two principal reasons. First, we have developed a global 3-D model of the crust and uppermost mantle that is designed to be used to predict regional travel times. We are unaware of any other 3-D global model that has been designed for this purpose. To predict reliable regional travel times from a global model requires careful attention to the crustal part of the model in order to reduce the crust-mantle trade-off that may bias the mantle part of the model. In addition, regional travel times are controlled largely by the turning point of the ray. The vertical gradient of the model, therefore, must be well determined. For regional travel times, the vertical resolution is probably more important than the lateral resolution of the model. Second, we have also developed a unique data base of nearly 1000 "Ground Truth" (GT) locations in 23 event clusters across much of Eurasia. These locations, together with the groomed arrival time data set and the empirical phase path anomalies that emerge for each cluster, provide invaluable information needed to determine the capability of any model or set of empirical travel time correction surfaces to predict regional travel times and locate seismic events using regional travel time data alone.

Improving the ability to locate regional events is important for two principal reasons. First, we believe that major improvements in global seismicity catalogs will derive principally through better use of regional data, at least for continental crustal events. As seismic networks proliferate, the quantity of regional data increases, but regional travel times are severely down-weighted in most global catalogs due to the inability of 1-D models to fit

these phases well and difficulties to identify phases reliably. The need for consistency in global catalogs has inhibited the adoption of modern models largely because 3-D model locations using teleseismic data provide only a moderate improvement over locations based on 1-D models. Thus, the ISC and the NEIS continue to use the Jeffreys-Bullen travel-time tables and the IDC uses the 1-D model IASP91 [*Kennett & Engdahl*, 1991]. Second, the concentration on monitoring efforts stimulated by the CTBT focuses attention on small events that may be clandestine nuclear explosions. Small events are recorded primarily at regional distances, perhaps with a few reported teleseismic phases. Moreover, the on-site inspection provisions of the treaty require the locations of these small events to be of high quality; semi-major axes of estimated error ellipses are specified to be less than 18 km. The focus of research efforts motivated by the technical requirements of the CTBT, therefore, is on regional locations with a sparse network of recording stations.

In section 2, we discuss the procedure used to construct the data base of GT locations, the groomed arrival time data set, and empirical phase path anomalies for each event cluster. The 3-D model construction and the ray-tracing procedure are discussed in section 4. The first test of the 3-D model is its ability to predict regional travel times. This is discussed in section 5 in which we discuss the fit to the empirical phase path anomalies. The second test of the 3-D model is the ability to locate the GT events using regional data alone. The grid-search location procedure is described in section 6 and the location tests are presented in section 7. We restrict the study to the use of P and P_n travel times for stations within 20° of the source locations. While optimal regional locations would include crustal phases, later P phases, and S phases, the consideration of these phases

is not necessary to test the performance of the 3-D model and, in fact, would complicate the interpretation of the location exercise.

2. Validating Data Set

2.1. Motivation

The assessment of a seismic velocity model requires a validating data set that is independent of the data used to derive the model. For this study, we have assembled a data set of seismic events with magnitudes above the IDC event definition threshold (currently $m_b \sim 3.75$) whose locations and origin times are known with greater than usual accuracy, either because they have been located with a local seismic network or because they were anthropogenic explosions. These so-called "Ground Truth" (GT) events are used to obtain reliable empirical estimates of source-station path anomalies (relative to a 1-D reference model) that can be compared with predictions from seismic models. The known locations of the GT events can also be compared to locations obtained from seismic models.

In this section, we discuss the development of the validating data set by multiple event relocation of clustered earthquake and explosion sequences in Eurasia and northern Africa. Primarily, we use phase arrival time data reported to the ISC and to the NEIS, but for some clusters we have obtained additional data (usually at regional distances) from other sources. The arrival time data are first "groomed" on an event by event basis, using a procedure described by *Engdahl et al.* [1998] in the development of the EHB catalog. A multiple event location method is then used to refine the locations and identify out-liers in the arrival time data. The resulting catalog of GT events, the groomed travel time data base, and the empirical phase path anomalies create a data base that can be used in experiments to assess 3-D models and to address systematic errors in event location.

The Ground Truth events occur in the clusters shown in Figure 1 and are listed in Table 1.

2.2. The GT Location Data Base

We seek clusters of earthquakes where at least one of the events has been very well located by a local seismic network or a temporary deployment of instruments, commonly in after-shock studies. We have used events from 1964-2001 in this study. The clusters typically are 50-100 km across and comprise up to about 100 events of magnitude 3.5 or greater that are well recorded at regional and teleseismic distances.

The multiple event location method used in this study is based on the Hypocentroidal Decomposition (HDC) method [*Jordan & Sverdrup*, 1981], which is schematically illustrated in Figure 2. This method uses projection operators to separate the location problem into two parts. The relative locations of events in the cluster are defined by "cluster vectors" in space and origin time, relative to the hypocentroid, which is defined as the geometric average of the absolute spatial and temporal coordinates of the cluster events at each iteration. The hypocentroid is then located in the traditional manner, as if all the data were from a single event. We use the 1-D model AK135 to locate the hypocentroid, to which the cluster vectors are added to yield absolute locations and origin times of all cluster events. The EHB single-event locations are used as the starting locations for the HDC analysis, which converges in several iterations. We perform HDC analysis many times on each cluster, however, in the process of identifying out-liers and estimating empirical reading errors.

Source depths are best estimated by local seismic networks, with at least one station whose epicentral distance is less than one source depth. This condition is rarely met, so

the depths for all events in this study were fixed in the HDC analysis. We fixed depths at the local network determination of focal depth for those events for which we have that information, and at an optimum depth (usually an average of the local network depths) for all remaining events in the cluster. To ensure that no gross errors in the assumed focal depths are made, we also examined reported depth phases at teleseismic distances [*Engdahl et al.*, 1998].

The absolute locations and origin times thus calculated are subject to bias from the use of a 1-D travel time model to locate the hypocentroid, just as single event locations are biased. The direction and degree of bias depend on the nature of departures of the 1-D model from the true velocity structure, combined with the particular distribution of observing stations. To minimize this bias, we shift the hypocentroid (i.e., the entire cluster) in space and time, as illustrated in Figure 2d, in order to provide an optimal match between the reference event locations and the corresponding cluster events. This brings all events in the cluster into close alignment with ground truth. We refer to the resulting set of 989 locations listed in Table 1 as the GT locations. The accuracy of the GT locations and the shift in the origin time ("cluster time baseline shift") are discussed further below.

For several reasons, P_n and P arrival time data were the primary phases used in the HDC analyses. First, they are ordinarily read as first arriving phases and are therefore more accurately picked. Second, at regional distances secondary phases usually arrive in the P_n/P coda, making them not only difficult to pick but also making it difficult to identify the phase type correctly. These difficulties arise mainly because, for most of the clusters studied, the propagation paths at regional distances for these phases pass

through regions of strong lateral heterogeneity, leading to complex waveforms. However, there are exceptions, such as propagation across the Indian Craton where S_n is observed as a coherent phase that can be read accurately; S_n was used in the analyses of the Bhuj and Chamoli clusters.

The reference event source parameters, which form the heart of the GT data base, were compiled from many sources, but were based exclusively on work done by the original investigators in each source region. We attempt to validate the claimed accuracy and assign a GT level of accuracy by analyzing the local network data and through tests of consistency with the HDC results. The epicenter accuracy of candidate reference events is first assessed on the basis of station geometry, described by fixed confidence bounds using a Ground Truth GTXC% classification, where the "X" suffix designates location accuracy in km and C% is the percent confidence [*Bondar et al.*, 2002]). For example, events that are accurate to within 5 km at a 95% confidence level are designated $GT5_{95\%}$. *Bondar et al.* [2002] argue that crustal events are located with 5 km accuracy or better at the 95% confidence level if they are located with (1) at least 10 stations within 250 km, (2) an azimuthal gap less than 110°, (3) a secondary azimuthal gap less than 160°, and (4) at least one station within 30 km of the epicenter. The final constraint provides some confidence in depth. Secondary azimuthal gap is defined as the largest azimuthal gap filled by a single station. In addition, it is desirable for local network solutions to be based on both $P-$ and $S-$wave arrival times and a local velocity model. For most clusters presented in this study, original documentation that included station locations, velocity model used, arrival times, and details of the solutions was compiled and carefully reviewed according to the above criteria.

We use "GT-level" classifications in two senses. First, is the sense of the accuracy level of individual reference events, as discussed above. Second, we use the same concept to describe the level of accuracy of entire clusters after shifting to best match the reference locations. The GT-level assigned to a cluster is more subjective, related to the GT-level of individual reference events, the number of reference events, the degree of consistency between the relative locations as expressed by the HDC analysis and reference data, and other factors. For example, the Aqaba cluster is calibrated by a single reference event, which qualifies as GT5, but we assign the cluster a GT10 level of accuracy because there is only a single reference event and because the event occurred in a region of very strong lateral heterogeneity, the transition from continental to oceanic lithosphere.

During the course of this study we discovered that many proposed reference events are in fact seriously mislocated. The consistency between the relative locations as determined by HDC analysis of global arrival time data and the relative locations derived from the reference event data is one of the criteria we use to validate candidate reference events. Shifts in epicenter and origin time to match the reference event locations are typically in the range of 5-15 km and ± 2 seconds, respectively.

We shift the hypocentroid in space and time to achieve the best fit for absolute locations and origin times between the HDC-derived locations and the reference event locations, as illustrated in Figure 2d. The "cluster time baseline shift" is the average difference between the reference event origin times and the origin times obtained by HDC analysis for those same events (Table 1). This correction is added to the HDC-derived origin times to produce a best estimate of absolute origin times. Positive corrections (i.e., shorter travel times) indicate faster velocities relative to AK135. The cluster time baseline shift

arises in part from differences between the 1-D model travel time used in the HDC analysis and the true travel times, but may also reflect bias in the reference event origin times. *Myers & Schultz* [2001] have shown that origin times estimated from local network data can be biased by several seconds if the local velocity model is not well-calibrated, even though the hypocenters may be estimated with high accuracy. The cluster time baseline shifts assist in phase identification and are also used to compare results between clusters and are included in estimates of empirical phase path anomalies relative to AK135, as discussed below.

Our HDC analyses are less afflicted by phase misidentification than single event locations for two reasons. First, the relative locations of cluster events are determined by differences in the travel time residuals, not their absolute value. Second, we use the information on cluster residuals (after average path error is removed and reading errors have been estimated), to identify out-liers which may be caused by phase identification errors. Phase misidentification remains as a problem for the estimation of the hypocentroid, but its influence is reduced by the much larger number of data used (several thousand), compared to most single event locations. In any case, the hypocentroid is ultimately shifted to match the reference event locations.

This method has resulted in a data base of 23 event clusters, including 6 explosion clusters with source locations generally known to better than 2 km, and 17 earthquake clusters, 11 of whose locations are believed to be accurate to within 5 km and the remainder to within 10 km. There are 989 GT events that compose these 23 clusters of which 753 are GT5 or better. The locations of the clusters studied are plotted in Figure 1. Relevant

parameters for all clusters are listed in Table 1. The location and depth given are for the shifted hypocentroid, representing the best fit to reference event locations.

2.3. The Groomed Arrival Time Data Set

A significant advantage of multiple event location, relative to single event location, is the opportunity to perform an iterative "grooming" process in order to identify and remove out-liers in the residuals until the normalized (by current assumed reading error), de-meaned residuals resemble a standard normal distribution. This results in a data set of groomed arrival times for each of the events in the GT data base. The number of these data is listed in Table 2 and Figure 3 shows a plot of the P_n and P residuals for all groomed arrival times included in this data base, adjusted by the cluster time baseline shift. Not unexpectedly, estimates of the residual median and spread show considerable variation over the regional distance range. In particular, residuals for P_n arrivals between about 9 and 17 degrees, corresponding to ray paths bottoming in the lithosphere well below the crust and perhaps encountering low velocity zones, are more spread, with a maximum spread at distances of 12-13 degrees. A contributing factor to this spread at larger regional distances is the difficulty of phase identification; e.g., distinguishing between various P_n branches or between P_n and P in regions where the crossover distance between the first-arriving branches of these phases is poorly known.

2.4. The Empirical Phase Path Anomalies

The basic premise of all multiple event location methods is that path anomalies from each station to all observed events in a given cluster are correlated. Thus, multiple event location analysis produces robust estimates of source-station path anomalies that

are far more difficult to extract from single event location catalogs. The set of groomed residuals for regional P and P_n, relative to shifted hypocenters derived by HDC analysis and adjusted for cluster time baseline shifts, are used to calculate source-station phase path anomalies. These anomalies are estimated relative to the 1-D reference model AK135. Medians and spreads for all groomed residuals for each cluster are calculated for all the phases of interest (P_g, P_n, P, S_g, S_n and S) at each of the reporting stations for that cluster. The resulting source-station "empirical phase path anomalies" (the median) are accepted with a minimum requirement of five observations and a spread of less than 1.40 sec and 2.8 sec for $P-$ and $S-$type phases, respectively. ("Spread" is a robust analog to the standard deviation.)

Ordinarily, there are too few P_g phases in the data base and the S-type phase residuals are too noisy to obtain useful results. At regional distances, however, there are 836 P_n and 178 P path anomalies, respectively. Results are plotted in Figure 4. These empirical estimates range from about -7.5 sec to +5.0 sec, with the largest anomalies occurring at distances from 11 to 18 degrees (similar to Figure 3). In this distance range, P_n typically has a triplication and P has a back branch (Figure 4b) making phase identification difficult.

3. Evaluation Metric

The method discussed in section 2 has produced three data sets that are useful for assessing 3-D seismic models. First, there is the set of 989 GT locations that are available to test location capabilities. In fact, only 753 of these events are identified as GT5 or better, and it is these events that will be most useful in this study. Second, there is the groomed travel time data, particularly regional P and P_n, from the ISC and NEIS

bulletins as well as some data from regional networks, that formed the basis for the HDC analyses. These data will be used to relocate the GT events in section 7 below. Finally, there are the empirical phase path anomalies that in section 5 are compared with the travel times predicted from several models (both 1-D and 3-D).

Studies aimed at evaluating the location capabilities of certain models or location techniques commonly concentrate exclusively on the accuracy of the locations relative to some benchmark. Although this is also an important part of the present study, we argue that the ability to model regional travel time data is a better measure of the quality of 3-D models and is, in fact, a more robust predictor of regional location capabilities. This is because evaluations based on location alone are complicated by a variety of factors that inhibit clear assessment; e.g., variations in network geometry from one region to another, different mixes of regional phases, differential quality of reported travel times, and so forth. The carefully constructed empirical phase path anomaly data set gives us confidence that assessments of the fit to regional travel time data provide meaningful, relatively unambiguous information about the quality of the models. The groomed travel time data set alone is probably too noisy to be used for this purpose.

4. 3D Model and Travel Time Computation

4.1. Model Construction

The 3-D model is based on broad-band surface wave group and phase speed measurements. The group velocities were measured using the method described by *Ritzwoller & Levshin* [1998], which is a frequency - time method that involves analyst interaction to choose the frequency band of measurement and to guide the extraction of the fundamental mode from noise, scattered and multipathed signals, overtones, and fundamental modes

of different wave types. We use group speed measurements from 16 s to 200 s period for Rayleigh waves and from 16 s to 150 s period for Love waves. The phase speed measurements were performed at Harvard University [*Ekström et al.*, 1997] and Utrecht University [*Trampert and Woodhouse*, 1995] separately and we merged these data sets. The phase speed measurements extend from 40 s to 150 s for both Rayleigh and Love waves. We use measurements only from earthquakes shallower than 50 km to reduce the size of the source group time shifts, which we do not attempt to correct [*Levshin et al.*, 1999]. All measurements are subjected to the quality control procedures described by *Ritzwoller & Levshin* [1998], but the number of group speed measurements has multiplied several times since that study.

The construction of the group and phase speed maps is founded on the tomographic method of *Barmin et al.* [2001], which is based on geometrical ray-theory with intuitive Gaussian smoothing constraints to simulate surface wave sensitivities. We refer to this method as Gaussian tomography. In fact we apply an update of this method [*Ritzwoller et al.*, 2002a], referred to as diffraction tomography, which uses a simplified version of the scattering sensitivity kernels that emerge from the Born or Rytov approximations. Diffraction tomography accounts for path-length-dependent sensitivity, wave-front healing and associated diffraction effects, and provides a more accurate assessment of spatially variable resolution than traditional tomographic methods. The resolution procedure is described by *Barmin et al.* [2001]. We produce a resolution surface at every nodal point on the globe, fit a cone to the surface in the neighborhood of each node, and define resolution as the half-width of the base of the cone (or identically, the full-width at half-max). Surface wave resolution estimates averaged over the region of study are presented

in Figure 5. Surface wave Fresnel zones widen appreciably at long periods and narrow only near sources and receivers, so resolution is best at short periods and in areas with sources or receivers.

The dispersion maps are produced on a $2^\circ \times 2^\circ$ grid world-wide. Diffraction tomography affects the amplitude and geometry of the dispersion features primarily at periods longer than about 100 s. As documented by *Ritzwoller et al.* [2002a], diffraction tomography, on average, produces larger anomalies in speed in a period-dependent band of spherical harmonic degrees, and diffraction and Gaussian tomography maps de-correlate past a critical spherical harmonic degree that also depends on period. Figures 6a and 6b show two examples of surface wave dispersion maps across the region of study constructed with diffraction tomography.

The shear velocity model is constructed using a Monte-Carlo method, which is described in detail by *Shapiro and Ritzwoller* [2002a]. The shear velocity model of *Shapiro and Ritzwoller* [2002a] was based on Gaussian tomography and is referred to here as CUB1.0. The 3-D shear velocity model we use here is based on diffraction tomography and we will refer to it as CUB2.0. These models only include v_p in the crust. The v_p part of CUB2.0 in the mantle will be derived by conversion from v_s using two different methods, and we will distinguish between these two v_p models by introducing suffices to the names (CUB2.0_TH, CUB2.0_EMP), as discussed below.

The inversion for a velocity profile is performed at each node on a $2^\circ \times 2^\circ$ grid world-wide, and produces an ensemble of acceptable models down to a depth of 400 km. The model is constrained by a variety of a priori information, including the initial crustal model CRUST2.0 (G. Laske, personal communication) and the initial mantle model S20A

of *Ekström & Dziewonski* [1998]. Perturbations are allowed within specified tolerances to both v_s and v_p in the crust, to v_s in the mantle, and to Moho depth. The model is radially anisotropic ($v_{sh} \neq v_{sv}$) from the Moho to a variable depth that averages about 200 km. The strength of radial anisotropy is constrained to decrease monotonically with depth and crustal speeds are constrainted to increase monotonically with depth. *Shapiro and Ritzwoller* [2002a] fully describes the set of constraints and a priori information.

Figure 7 presents an example of the results of the Monte-Carlo inversion at a single point. The center and half-width of the ensemble of acceptable models summarize the model at each depth. The effective isotropic model, v_s, is defined as the average of v_{sh} and v_{sv} at each depth. Figures 7b-d show that model uncertainties are reduced and, hence, vertical resolution is improved appreciably by simultaneously inverting the group and phase speed curves. Using phase velocities alone produces large uncertainties in the crust and, consequently, also in the upper mantle. Inverting group velocities alone reduces the uncertainties in the crust and uppermost mantle due to the measurements at periods shorter than 40 sec, but uncertainties deeper in the upper mantle are larger. When phase and the group velocities are inverted simultaneously, however, uncertainties are significantly reduced at all depths. In particular, the simultaneous inversion of broad-band group and phase speed data in the presence of a priori constraints on allowable structures in the crust and upper mantle ameliorates the trade-off between crustal and upper mantle structures that plague inversions of surface waves in continental areas.

Figures 6c-d and 8b-c present horizontal and vertical slices of the v_s model to demonstrate the nature of the heterogeneities. It is noteworthy that the mantle features inferred from diffraction tomography tend to have larger amplitudes and extend deeper than those

from Gaussian tomography. Based on the dispersion resolution information given in Figure 5, we infer that average lateral resolution is between 400 and 500 km in the uppermost mantle but degrades with depth. As length-scales in the model approach the estimated resolution, however, the amplitude of heterogeneity will tend to become underestimated.

4.2. Conversion of v_s to v_p in the Mantle

To be able to predict P_n and P travel times, the 3-D S-model CUB2.0 must be converted to a P-model. There are two general approaches to doing this. The first is to use "empirical scaling relations" that convert S-wave anomalies into P-wave anomalies. The most successful of these, map shear-speed perturbations, δv_s, relative to a reference S-model, v_{s_0}, to compressional-velocity perturbations, δv_p, relative to a reference P-model, v_{p_0}, where $d\ln v_p/d\ln v_s$ is then taken to be an empirically constrained constant that may be a function of depth, but is usually depth invariant. The second approach is to use a "theoretical conversion" based on laboratory measurements of thermoelastic properties of mantle minerals and on models of the average mineralogical composition of the mantle. The v_p model that results from CUB2.0 v_s by the theoretical conversion will be referred to here as CUB2.0_TH and the v_p model derived from the empirical scaling relation ($d\ln v_s/d\ln v_p = 1.9$) in which the 1-D reference model is AK135 will be called CUB2.0_EMP. We convert only isotropic v_s to v_p. In the radially anisotropic part of CUB2.0 we, therefore, use $(v_{sv} + v_{sh})/2$.

We prefer the theoretical conversion from v_s to v_p for two reasons. First, as we will show below, the theoretical conversion appears to work somewhat better in that the regional P and P_n empirical phase path anomalies are fit better by travel times predicted by CUB2.0_TH than by CUB2.0_EMP. Second, the theoretical conversion leads naturally

to future improvement. It can be regionally tuned in a physically meaningful way by modifying the mineralogical composition and temperatures within the anelastic model, and it can be updated as better mineralogical data become available.

The theoretical conversion between v_s and v_p in the mantle is mediated by a conversion to temperature. There have been numerous previous studies that have explored the relationship between the seismic velocities, temperature, and composition [e.g., *Duffy & Anderson*, 1989; *Graham et al.*, 1989; *Furlong et al.*, 1995; *Sobolev et al.*, 1996; *Goes et al.*, 2000; *Röhm et al.*, 2000; *Trampert et al.*, 2001; *van Wijk et al.*, 2001]. The method we use here is based on that of *Goes et al.* [2000], and is described in detail by *Shapiro and Ritzwoller* [2002b]. The mantle is considered to be composed of four principal minerals. The elastic moduli and density can be computed for each mineral independently as a function of temperature, pressure, and iron content, extrapolating values of each quantity at surface conditions to depth with zero iron content by using experimentally-determined partial derivatives. For a specific mineralogical composition, the elastic moduli and density, and hence the seismic velocities, are computed using the Voigt-Reuss-Hill mixing scheme. The result holds at high frequencies or very low temperatures where anelasticity contributes minimally. At mantle temperatures and seismic frequencies, however, the temperature-velocity relation must include a correction for physical dispersion. Because upper-most mantle Q is poorly known, we use the attenuation model of *Minster & Anderson* [1981] that relates Q to temperature. We follow *Sobolev et al.* [1996] in specifying the parameters in this conversion (frequency exponent, activation energy and volume), but we calibrate the amplitude of the correction based on the average shear-velocity in the region of study and an assumed average upper mantle temperature of 1400°C at 200

km depth. We use a single mineralogical composition here for the entire region of study, the average off-cratonic continental composition advocated by *McDonough & Rudnick* [1998]: 68% Olivine, 18% Orthopyroxene, 11% Clinopyroxene, and 3% Garnet with an Iron:Magnesium ratio of 10%.

Figure 9a shows the resulting v_s to v_p theoretical conversion. Figure 9b displays this conversion presented as the logarithmic scaling relation, $d\ln v_s/d\ln v_p$, which varies with both v_s and depth. The v_s profile from AK135 is overplotted, nearly paralleling the contours of the theoretical predictions. This illustrates why depth-independent values of the scaling relation tend to work fairly well in the upper mantle. For the values of v_s in AK135, the theoretical prediction for the scaling relation is $d\ln v_s/d\ln v_p \sim 1.6 - 1.8$. Figure 9b also shows that the v_s profile converted from the AK135 v_p profile by the theoretical conversion agrees fairly well with the v_s profile in AK135 at depths below about 100 km. The theoretical conversion between v_s and v_p differs appreciably from the v_s and v_p parts of AK135 above about 100 km. Thus, in the shallower parts of the mantle, v_p computed using the theoretical conversion will differ appreciably from v_p computed using the logarithmic scaling relation applied to reference values from the 1-D model AK135. Figure 10a exemplifies this by showing representative v_p profiles from tectonic (e.g., $A - A'$) and platform (e.g., $B - B'$) regions of CUB2.0_TH and CUB2.0_EMP.

4.3. Travel Times and Correction Surfaces

To compute travel times for P_n and P we use a modified version of the 2-D ray tracer developed by *Červený & Pšenčík* [1984]. *Villaseñor et al.* [2002] shows that this code applied to the CUB 3-D models agrees well with travel times from the finite difference code of *Podvin & Lecomte* [1991] modified to be applied on a spherical earth. They also

show that travel time variations from 3-D excursions in regional rays through the CUB 3-D models are small and do not substantiate the computational cost of computing 3-D rays. Even in 2-D, P_n is a very complex phase as the rays and travel time curves shown in Figure 11 illustrate.

The travel times of the P_n phase from the 3-D P-models derived with the two conversion schemes can differ appreciably, as Figure 12 shows. In a geographically averaged sense, CUB2.0_EMP produces P_n travel times that are about 1 sec faster than P_n times from CUB2.0_TH. This discrepancy is strongest in tectonic areas, but in shield areas the theoretical conversion actually tends to produce faster times at distance beyond about 100 km because the deeper parts of the model beneath the shallow mantle lid are faster and rays tend to dive deeper. The difference between the empirical and theoretically converted P_n travel times is largest at distances beyond about 2000 km. This is probably because second-order pressure dependencies are needed in the theoretical conversion for rays turning deeper than about 250 km. Future advances in the theoretical conversion based on finite-strain theory may correct this effect, but for the present study it is a moot point, at least for P_n, which is rarely observed beyond 2000 km. The use of the theoretical conversion for longer baseline P phases, however, will need to take this into consideration.

For the validation exercises in later sections, we compute "travel time correction surfaces" for P_n and P for all of the 854 stations in the groomed arrival time data set. Separate surfaces are computed for a discrete set of hypothesized event depths (0, 10, 20, 30, 40 km) and are then interpolated to provide correction surfaces for events between this set of depths. These travel time surfaces depict the predicted travel times from events on a grid of epicentral locations and depths observed at a particular station, and are pre-

sented relative to the travel time predicted from a 1-D model. Figure 13 presents examples of regional station-centered travel time correction surfaces for P and P_n computed from CUB2.0_TH relative to the travel times from IASP91. Figure 14 presents examples of event-centered correction surfaces relative to travel times from AK135.

5. Fit to Regional Travel Times

The first assessment of the 3-D model is to determine how well regional travel times predicted by the 3-D P-wave models CUB2.0_TH and CUB2.0_EMP fit well determined regional travel time observations. This test is made possible by the empirical phase path anomaly data set described in section 2. We compute travel times from each model tested by using the GT locations, depths, and origin times. We will argue that the systematics of misfit establish that the 3-D model greatly improves the fit to regional travel times over 1-D models and that the theoretical conversion from v_s is preferable to the empirical scaling relation.

We perform comparisons both cluster-by-cluster and aggregated over clusters, segregating the results by event type (e.g., explosions, GT5 or GT10 earthquakes). Examples of cluster-specific comparisons are presented in Figures 14 and 15. In each case, we allow an offset to the predicted correction surface to minimize the rms travel time residual. A similar shift was also introduced in the HDC analysis and in the construction of the empirical phase path anomalies discussed in section 2, referred to as "cluster time baseline shifts". These shifts are listed in Table 1 in which the 1-D model AK135 and both regional and teleseismic data were used. Using just regional data, they are listed in Tables 3 - 5 for the 3-D model CUB2.0_TH and the 1-D model AK135. Tables 3 - 5 also provide information about misfit and correlation between the model predicted travel times and the empirical

phase path anomalies. Note that correlation is defined with respect to perturbations relative to AK135. The correlation of AK135 travel times with the empirical phase path anomalies is zero, therefore, because the perturbations are all zero. For this reason, the correlations for AK135 are left out of Tables 3 - 5.

Figure 14 presents examples of cluster-centered travel time correction surfaces produced from CU2.0_TH with the empirical path anomalies for P_n overlain. Plots such as these establish the qualitative agreement between the empirical path anomalies and the model predicted travel times, at least with respect to the large-scale features of the correction surfaces. More quantitative comparisons are seen in Figure 15, which also demonstrates the effect of phase re-identification using the 3-D model. Aggregated comparisons, such those shown in Figure 16 and the averages presented in Tables 3 -5, demonstrate that the model fit to the empirical path anomalies depends strongly on the GT level, with explosions being fit best, followed by GT5 and finally GT10 earthquakes. Figures 15 and 16 display as dashed lines the ± 3 sec residual levels to demonstrate that misfits at this level are rare, especially for explosions. In the location exercise below, we will, therefore, use ± 3 sec as the cut-off for out-lier identification. Residuals with absolute values greater than 3 sec are suspicious measurements or are phases that are particularly difficult to identify.

The rms-misfit averaged over the explosion clusters for CUB2.0_TH is about 1.04 sec, and misfit averaged over the GT5 and GT10 earthquake clusters averages 1.24 sec and 1.54 sec, respectively. These values are to be contrasted with misfit using the 1-D model AK135: 1.70 sec, 1.70 sec, and 2.10 sec, respectively. The 3-D model, therefore, delivers a 64% variance reduction relative to the 1-D model for the explosions and a 46% variance

reduction for the earthquakes. The fact that the GT level affects the fit to the regional travel times is not surprising, but does lend support to the procedure that established the GT-level discussed in section 2.

Tables 3 - 5 also list the cluster time baseline shifts for CUB2.0_TH and AK135 using the regional empirical phase path anomalies alone (i.e., in contrast to Table 1 in which teleseismic travel times were used). The cluster time baseline shifts are introduced to compensate for origin time errors in the GT data base and to aid in phase identification, but they also act to correct model errors in both the crust and uppermost mantle, particularly beneath the cluster. Tables 3 - 5 show that, on average, the cluster time baseline shifts are systematically smaller for CUB2.0_TH than for AK135 (explosions: 1.04 sec versus 2.09 sec; GT5 earthquakes: 0.76 sec versus 1.44 sec; GT10 earthquakes: 0.28 sec versus 1.43 sec). In fact, they are smaller for all but two of the clusters which have anomalously small shifts for the 1-D model. This is presumably because the 3-D model CUB2.0_TH more accurately models near-cluster structure than the 1-D model AK135. (Results are not presented for the Aden or Sahara clusters because there are too few regional data for meaningful statistics.)

Because the cluster time baseline shifts may obscure some problems with the model, it is also important to perform travel time comparisons without the shifts. Figure 17 compares the empirical P and P_n path anomalies with the travel times predicted by a number number of models (1-D: AK135, PREM; 3-D: CU2.0_TH, CU2.0_EMP, AK135+CRUST5.1+S20A_TH) as a function of epicentral distance. The model AK135+CRUST5.1+S20A_TH is a v_p model of the crust and mantle constructed by placing CRUST5.1 [*Mooney et al.*, 1998] on top of P-wave speeds converted from the

3-D mantle v_s model S20A [*Ekström & Dziewonski*, 1998]. The model S20A was, in fact, developed as an aspherical perturbation to PREM, but because PREM was not developed to fit regional travel times, we replace it with AK135 as the spherical reference for this model. Finally, we use the theoretical conversion from v_s to v_p to compute the v_p part of the mantle model; hence the suffix on the name AK135+CRUST5.1+S20A_TH.

Figures 17a - 17e show residuals for every empirical path anomaly in the data base. These residuals are averaged in distance bins and broken into a vertical offset (or bias) and the standard deviation around the offset as shown in Figures 17f and 17g. We divide the comparison in this way because it is possible for a model to fit the geographical pattern of travel time residuals well but be systematically biased. The overall rms-residual would, therefore, be large, but that alone would provide little insight into the reason behind the large residuals.

Figures 17f and 17g demonstrate that the 1-D model AK135, which was constructed to fit regional travel times on average, fits the empirical path anomalies better than PREM, which displays a bias of about 4 sec at distances less than 1500 km. This is largely due to thin crust in PREM ($\sim$20 km after the ocean was removed for continental application). The travel times from AK135 are also biased, but at a lower level than PREM, and the distance trend is less severe. The pattern of bias for CUB2.0_EMP reflects the bias in AK135, probably because of the reliance of the empirical v_s to v_p conversion on AK135. The travel times from the two 3-D models that have been converted to v_p with the theoretical conversion (CUB2.0_TH, AK135+CRUST5.1+S20A) are much less biased. This is one of the reasons for our preference for the theoretical v_s to v_p conversion. We will, thereforem, not consider CUB2.0_EMP in the location exercises below.

The fit to the geographical pattern of empirical phase path anomalies is revealed in the standard deviation shown in Figure 17g. The 3-D models all fit better than the 1-D models. CUB2.0_TH has only a slightly smaller standard deviation than CUB2.0_EMP. CUB2.0_TH fits the pattern of empirical phase path anomalies somewhat better than AK135+CRUST5.1+S20A. This is a promising because CUB2.0_TH was built by perturbing AK135+CRUST5.1+S20A. This perturbation was accomplished by introducing many regional group speed measurements in the attempt to improve lateral and, more importantly, vertical resolution in the resulting model (e.g., Figure 7). There was no guarantee that this procedure would produce a v_p model that would improve the fit to regional P-phases, but these results establish that it has. This points the way to future advancements in v_s models providing further improvements in regional location capabilities.

6. Location Method

We developed a grid-search location method to be used in the second assessment of the 3-D model. In addition to the three principal unknowns, origin time (t_0), depth (z), and epicentral location (x, y), we consider phase identification to be unknown. We will fix the depth because it trades off with origin time and fixing it has little effect on the epicentral location. To simplify the inversion, we re-identify phases only at the grid-center rather than at each grid node separately, and use only P_n and P data observed between $\sim 3^\circ$ and 20°. The use of S_n and S travel times would improve the locations, particularly for locations with few reporting stations. The quality and distribution of reported regional S-phases, however, are much more variable than P-phases and their use would make the results more difficult to interpret. These simplifications result in much more stable

location results, but the location method differs substantially from procedures that are used to construct global catalogs. Thus, our reports of location capabilities are probably more meaningful in a relative sense (e.g., location error with the 3-D model relative to the 1-D model location) than an absolute sense. The 3-D model that is tested here is CUB2.0_TH and the 1-D model is AK135.

The location procedure progresses in five steps. (1) **Fix event depth.** The depth z is fixed to the value in the GT location data base. (2) **Create the grid.** The grid is chosen with the grid-center at the EHB location for earthquakes and the PDE location for explosions, and nodes are located every 1 km to create a 50 km $\times$ 50 km grid. The PDE location is chosen for the grid-center for explosions because the EHB location for explosions is commonly of GT0-2 quality, which would create an asymmetry between earthquakes and explosions. The EHB and PDE locations are probably more accurately characterized as GT10 - GT15. (3) **Phase identification and origin time.** With a hypothesized epicenter at the grid-center, each travel time is identified as either P or P_n and the origin time is shifted (relative to an input estimate) to give the smallest over-all rms-residual. (4) **Out-lier rejection.** Residuals larger than ± 3 sec using the 3-D model are considered to be out-liers and are rejected. The 3 sec criterion is based on fits to the empirical phase path anomalies (e.g., Figure 16). It is about the 3σ level for explosions and 2σ for earthquakes. The details of this choice have little effect on the overall statistics because the number of observations that are rejected is small. In principal, this procedure could be performed separately at each grid node. This would, however, produce different data sets for each model, which would complicate interpretion of the results. We also believe that the 3-D model accurately identifies erroneous measurements. (5) **Epicenter**

estimate. Hypothetical epicenters are moved to each grid node and the estimated event location is identified with the grid node that produces the minimum misfit to the observed travel times in the groomed arrival time data set.

An example of the location grid for an explosion on the Lop Nor test site is shown in Figure 18.

7. Regional Location Experiment

The location experiment is performed using only P and P_n travel times from the groomed arrival time data set, observed within 20° of the epicenter. The figure-of-merit is the ability to locate those events in the GT data set with location accuracy of GT5 or better. We compare the location capabilities of the 3-D model CUB2.0_TH to that of the 1-D model AK135. Examples of locations using these models are shown in Figure 19 for the Lop Nor and Racha clusters. Qualitatively, it can be seen that the 3-D model improves the agreement with the GT locations and reduces systematic bias.

The geometry of the network of reporting stations plays a major role in location accuracy. Figure 20 presents examples of how location error varies with the number of stations and open azimuth. These results are determined by performing locations repeatedly using randomly chosen subsets of the reported data in the groomed arrival time data set with a specified number of recording stations. The location systematics for the 3-D model are clear and reasonable: as the number of stations decreases and open azimuth increases the location accuracy degrades. We aim, however, for the statistics on location accuracy to reflect the capabilities of the model rather than the vagaries of station geometry. It is, therefore, important to limit the role that variations in network geometry between different event regions play on the reported locations. For this reason, the location statistics

reported in Tables 6 - 8 are only for the GT events with open azimuths less than 180° for regional P and P_n data. This reduces the GT data set by more than 60%, from 989 to 366 events. The number of explosions is most severely reduced, from 312 to 38 events, but the number of events remains high enough to draw statistically meaningful conclusions.

Using the 3-D model, the location accuracy improves systematically with the confidence in the GT location: 5.1 km, 7.2 km, and 12.3 km errors for explosions (GT0-GT2), GT5 earthquakes, and GT10 earthquakes, respectively. By the following reasoning, we believe that these results are consistent with an intrinsic location accuracy of about 5 km for the 3-D model. Assuming that the regional location errors and the reported GT confidence levels are uncorrelated, we would expect a location error of about $(5^2 + 5^2)^{1/2}$ km ~ 7 km for GT5 events if the intrinsic location error is itself 5 km, and $(10^2 + 5^2)^{1/2}$ km ~ 12 km for GT10 events. These expectations are very similar to to the results of our tests, and give us further confidence in the GT levels reported in Table 1.

Location errors for the 1-D model do not trend as simply with GT level. Location errors are 14.1 km, 10.9 km, and 13.3 km, respectively, for explosions, GT5 earthquakes, and GT10 earthquakes. The location error for the explosions is elevated by the difficulties that the 1-D model has in locating the Azgir events. The reason is the nature of the 3-D structure near Azgir: fast continental platforms to the north and slow tectonic regions to the south. The 3-D model corrects for this large-scale variability very well, but the 1-D model produces systematically biased locations similar to its performance at Racha (Figure 19d). It is, nevertheless, reasonable to conclude that the 1-D model possesses an average intrinsic location accuracy of about 10 km from which we would expect estimated location errors of about 10 km, 11 km, and 14 km, respectively, for explosions, GT5

earthquakes, and GT10 earthquakes. This accuracy is much more geographically variable than for the 3-D model, however.

These estimates of intrinsic location accuracies (5 km for the 3-D model, 10 km for the 1-D model) have been determined for relatively large events for which a large number of regional phases were available. It is important in a number of applications, particularly in nuclear monitoring, to understand how location accuracy degrades as the network of recording stations becomes increasingly sparse. Figure 21 addresses this question by considering location accuracy as a function of random subsets of the reported stations. The approach is similar to that taken in Figure 20, but here we have aggregated the results over different types of events: explosions in Figure 21a and GT5 events in Figure 21b. The averages and standard deviations of the distributions of locations are presented as a function of the number of stations retained, with the constraint that open azimuth remains less than 180°. Note that explosion locations for the 3-D model degrade from about 5 km using a large number of stations to about 8 km on average for 5 reported stations. GT5 earthquake locations using the 3-D model similarly degrade from averages of about 11 km to 17 km. Figures 21a and 21b also show that (1) the average location error grows as the number of stations decreases with degradation setting on at about 10 stations, (2) the mean and standard deviation of the distributions are smaller for the 3-D model than for the 1-D model, and (3) the mean and standard deviation are smaller for explosions than for GT5 earthquakes.

What is not shown in Figures 21a and 21b is that the distributions of location error for the two models are highly correlated. Therefore, even though the location error distributions for the two models for the GT5 earthquakes overlap appreciably, the 3-D model

location is better than the 1-D model location in no less than 70% of the cases considered. For the GT5 earthquakes, this number remains approximately constant with the number of reporting stations. For the explosions, however, it degrades from more than 90% for large numbers of stations used to about 75 - 80% % for sparse networks containing less than 10 regional stations.

8. Discussion

The validation tests reported above yield a number of general lessons that we discuss further here.

8.1. GT Data Bases

Data bases of earthquake and explosion locations with high accuracy and quantified uncertainties (Ground Truth data bases) provide valuable information needed to test earth models and to determine seismic location capabilities. Such data bases are very difficult to assemble, however, as they require substantial efforts to validate. The Hypocentroidal Decomposition (HCD) method of multiple event location, in particular, is very well suited to the requirements of Ground Truth (GT) validation exercises. The empirical phase path anomalies that can be constructed from clusters of events provide important ancillary information about the capabilities of earth models.

It is a popular conception that compilations of regional empirical phase path anomalies may be used directly to construct empirical "correction surfaces" to be used in location procedures. Our experience is that information of GT10 quality or better results only after strenuous efforts, and accrues only in isolated regions of the globe where reference events are available. It is not likely, therefore, that empirically-derived regional correction

surfaces can be developed from GT10 data bases in a general sense. It remains to be determined if empirical correction surfaces that derive from lower quality locations will be able to perform as well as existing 3-D earth models, such as CUB2.0_TH, over large, diverse, and widely dispersed regions. It is, for example, still not fully understood how best to merge model predictions with empirical path corrections. We have shown here that high quality baseline information from existing 3-D models exists already, and provides a context into which empirical information of similar quality can be introduced in the future.

8.2. *S*-Wave Models

The 3-D models tested here (CUB2.0, S20A) are, in essence, v_s models of the upper mantle that have been derived largely from information about surface wave dispersion. Surface waves possess the salutary characteristic that they sample the entire earth, and over large regions data coverage is dense and relatively homogeneous. Another advantage is that broad-band surface wave dispersion constrains the vertical velocity gradient in the upper mantle. The vertical gradient controls ray turning depths which, in turn, largely control travel times.

It is much more difficult to constrain 3-D models of v_p in the uppermost mantle directly, except in rare regions with exceptional station coverage and seismicity. P_n tomography produces 2-D surfaces which provide no information about the vertical velocity gradient generally needed to predict regional travel times. P_n tomographic maps have been shown by *Ritzwoller et al.* [2002b] to correlate well with uppermost mantle P-wave velocities computed from earlier v_s models of Eurasia [*Villaseñor et al.*, 2001], but it is not yet clear how to assimilate information from P_n tomography into 3-D models. This is exacerbated

by the fact that P_n is a very complicated phase, whose general characteristics exhibit substantial regional variation (e.g., number and location of triplications). It is, therefore, noteworthy that the 3-D v_p models that we construct from v_s fit regional P-wave travel times well and improve regional location capabilities relative to 1-D models, such as AK135, that have been constructed using regional P-wave data.

The quality of S-wave models of the mantle has been improving rapidly over the past few years. Continued improvement, therefore, promises to advance location capabilities further. For example, the model CUB2.0 was constructed by perturbing the Harvard model S20A in order to fit a large new data base of regional group speed measurements in the attempt to improve lateral and, more importantly, vertical resolution in the resulting model. There was no guarantee that this procedure would produce a v_p model that would improve the fit to regional P-phases, but it clearly does. Future advancements in v_s models, both through theoretical developments as well as the assimilation of a variety of data that have hitherto not been used (e.g., heat flow, *Shapiro and Ritzwoller* [2002b]; receiver functions, *Julia et al.* [2000]), will provide a natural path to further improvements in regional location capabilities.

8.3. Importance and Promise of the "Theoretical" v_s to v_p Conversion

The conversion of v_s to v_p has been a major stumbling block to adopting global 3-D seismic models as part of both teleseismic and regional location methods. Recent advances in mineral physics have greatly improved the theoretical conversion of v_s to v_p. Continued improvements in the theory (e.g., finite strain theory) as well as developments in ancillary information (e.g., information about the upper mantle composition) can be incorporated naturally into this conversion scheme. In addition, the conversion can be

tuned regionally, by varying mantle composition, and optimizing the anelastic correction as well as other parameters in the conversion. To date, we have applied the v_s to v_p conversion directly from the mineral physics literature. Empirical phase path data sets, in particular, could be used to tune the conversion by optimizing certain parameters that are set in the conversion. These factors argue that the theoretical conversion from v_s to v_p provides a promising basis for future improvements in regional location capabilities based on 3-D seismic models.

Acknowledgments. We gratefully acknowledge the staffs at the IRIS-DMC and the GEOFON and GEOSCOPE data centers for providing most of the waveform data on which the 3-D model is based. We are also particularly grateful to Jeannot Trampert at Utrecht University and Michael Antolik, Goran Ekström, and Adam Dziewonski at Harvard University for providing phase speed measurements. The ray tracing software was written by Mikhail Barmin. Istvan Bondar, Joydeep Bhattacharyya, Vadim Levin, and Antonio Villaseñor provided useful feed-back on its use. All maps were generated with the Generic Mapping Tools (GMT) data processing and display package (Wessel and Smith, 1991, 1995). This work was supported by contracts from the Defense Threat Reduction Agency, contracts DTRA01-99-C-0019, DTRA01-00-C-0013, and DTRA 01-00-C-0032.

References

Antolik, M., G. Ekström, and A.M. Dziewonski, Global event location with full and sparse data sets using three-dimensional models of mantle P-wave velocity, *Pure Appl. Geophys.*, *158*, 291-317, 2001.

Barmin, M.P., A.L. Levshin, and M.H. Ritzwoller, A fast and reliable method for surface wave tomography, *Pure Appl. Geophys.*, *158*, 1351-1375, 2001.

Bijwaard, H., W. Spakman, and E.R. Engdahl, Closing the gap between regional and global travel time tomography, *J. Geophys. Res., 103*, 30,055-30,078, 1998.

Bondar, I., S.C. Meyers, E.R. Engdahl and E.A. Bergman, Epicenter accuracy based on seismic network criteria, in preparation, 2002.

Boschi, L. and A.M. Dziewonski, High and low-resolution images of the Earth's mantle: Implications of different approaches to tomographic modeling, *J. Geophys. Res., 104*, 25,567-25,594, 1999.

Červený, V., and I. Pšenčík, SEIS83 – Numerical modeling of seismic wave fields in 2-D laterally varying layered structures by the ray method, it Documentation of earthquake algorithms, Report SE-35, E.R. Engdahl (ed.), pp. 36-40, Boulder: World Data Center A for Solid Earth Geophysics, 1984.

Chen, Q.-F. and R.J. Willemann, Global test of seismic event locations using three-dimensional earth models, *Bull. Seismol. Soc. Am., 91*, 1704-1716, 2001.

Duffy, T.S. & Anderson, D.L., Seismic velocities in mantle minerals and the mineralogy of the upper mantle, *J. Geophys. Res., 94*, 1895-1912, 1989.

Dziewonski, A.M. and D.L. Anderson, Preliminary reference earth model, *Phys. Earth Planet. Inter., 25*, 297-356, 1981.

Ekström, G. & Dziewonski, A.M., The unique anisotropy of the Pacific upper mantle, *Nature*, *394*, 168-172, 1998.

Ekström, G., Tromp, J., & Larson, E.W.F., Measurements and global models of surface waves propagation, *J. Geophys. Res., 102*, 8137-8157, 1997.

Engdahl, E. R., R. van der Hilst, and R. Buland, Global teleseismic earthquake relocation with improved travel time and procedures for depth determination, *Bull. Seismol. Soc. Am., 88*, 722 - 743, 1998.

Firbas, P., Location calibration based on 3-D modelling: Steps towards the calibration of the global CTBT network, in *Advances in Seismic Event Location*, edited by C.H. Thurber and N. Rabinowitz, pp. 135-161, Kluwer Acad. Publ., Netherlands, 2000.

Furlong, K.P., Spakman, W., and Wortel, R., Thermal structure of the continental lithosphere: constraints from seismic tomography, *Tectonophys., 244*, 107-117, 1995.

Geiger, L., Probability method for the determination of earthquake epicenters from the arrival time only, *Bull. St. Louis University, 8*, 60-71, 1912.

Goes, S., Govers, R., & Vacher, R., Shallow mantle temperatures under Europe from P and S wave tomography, *J. Geophys. Res., 105*, 11,153-11,169, 2000.

Graham, E.K., B. Yan, and K.P. Furlong, Lateral variations in upper mantle thermal structure inferred from three-dimensional seismic inversion models, *Geophys. Res. Lett.,* **16**, 449-452, 1989.

Jeffreys, H. and K.E. Bullen, *Seismological Tables*, British Association for the Advancement of Science, London, 1940.

Jordan, T.H. and K.A. Sverdrup, Teleseismic location techniques and their application to earthquake clusters in the south-central Pacific, *Bull. Seismol. Soc. Am., 71*, 1105-1130, 1981.

Julia, J., C.J. Ammon, R.B. Herrmann, and A.M. Correig, Joint inversion of receiver function and surface wave dispersion observations, *Geophys. J. Int., 143*, 99-112, 2000.

Kennett, B.L.N. and E.R. Engdahl, Traveltimes for global earthquake location and phase identification, *Geophys. J. Int., 105*, 429-465, 1991.

Kennett, B.L.N., E.R. Engdahl, and R. Buland, Constraints on seismic velocities in the Earth from travel times, *Geophys. J. Int., 122*, 108-124, 1995.

Levshin, A.L., M.H. Ritzwoller, and J.S. Resovsky, Source effects on surface wave group travel times and group velocity maps, *Phys. Earth Planet. Inter., 115*, 293 - 312, 1999.

McDonough, W.F. & Rudnick, R.L., *Mineralogy and composition of the upper mantle*, in: Ultrahigh-pressure mineralogy: physics and chemistry of the Earth's deep interior, R.J. Hemley, Editor, Mineralogical Society of America, Washington, DC, 1998.

Minster, J.B. & Anderson, D.L., A model of dislocation-controlled rheology for the mantle, *Philos. Trans. R. Soc. London, 299*, 319-356, 1981.

Mooney, W.D., G. Laske, and G. Masters., CRUST5.1: A global model at 5 degrees by 5 degrees. *J. Geophys. Res., 102*, 727-748, 1998.

Myers, S.C., and C.A. Schultz, Improving sparse network seismic location with Bayesian Kriging and teleseismically constrainted calibration events, *Bull. Seismol. Soc. Am., 90*, 199-211, 2000.

Myers, S.C., and C.A. Schultz, Statistical characterization of reference event accuracy (abstract), *Seismol. Res. Lett.*, 72, 244, 2001.

Piromallo, C. and A. Morelli, Improving seismic event location: An alternative to three-dimensional structural models, *Pure Appl. Geophys.*, *158*, 319-347, 2001.

Podvin, P. and I. Lecompte, Finite difference computation of travel times in very contrasted velocity models: a massively parallel approach and its associated tools, *Geophys. J. Int., 105*, 271-284, 1991.

Ringdal, F. and B.L.N. Kennett, (Eds.), Monitoring the Comprehensive Nuclear-Test-Ban Treaty: Source Location, *Pure Appl. Geophys.*, *158*(1-2), pp. 428, 2001.

Ritzwoller, M.H. and A.L. Levshin, Eurasian surface wave tomography: Group velocities, *J. Geophys. Res., 103*, 4839-4878, 1998.

Ritzwoller, M.H., N.M. Shapiro, M.P. Barmin, and A.L. Levshin, Global surface wave diffraction tomography, *J. Geophys. Res.,* in press, 2002a.

Ritzwoller, M.H., M.P. Barmin, A. Villasenor, A.L. Levshin, and E.R. Engdahl, P_n and S_n tomography across Eurasia, *Tectonophys.*, in press, 2002b.

Röhm, A.H.E., Snieder, R., Goes, S., & Trampert, J., Thermal structure of continental upper mantle inferred from $S-$wave velocity and surface heat flow, *Earth Planet. Sci. Lett., 181*, 395-407, 2000.

Schultz, C.A., S.C. Myers, J. Hipp, and C.J. Young, Nonstationary Bayesian kriging: A predictive technique to generate spatial corrections for seismic detection, location, and identification, *Bull. Seismol. Soc. Am., 88*, 1275-1288, 1998.

Shapiro, N.M. and M.H. Ritzwoller, Monte Carlo inversion for a global shear velocity model of the crust and upper mantle, *Geophys. J. Int.*, in press, 2002a.

Shapiro, N.M. and M.H. Ritzwoller, Thermodynamic constraints on seismic inversions, *Geophys J. Int.*, submitted, 2002b.

Smith, G.P. and G. Ekström, Improving teleseismic event locations using a three-dimensional earth model, *Bull. Seismol. Soc. Am., 86*, 788-796, 1996.

Sobolev, S.V., Zeyen, H., Stoll, G., Werling, F., Altherr, R., & Fuchs, K., Upper mantle temperatures from teleseismic tomography of French Massif Central including effects of composition, mineral reactions, anharmonicity, anelasticity and partial melt. *Earth*

Planet. Sci. Lett., 157, 193-207, 1006, 1996.

Su, W.-J., R.L. Woodward, and A.M. Dziewonski, Degree 12 model of shear velocity heterogeneity in the mantle, *J. Geophys. Res., 99*, 6945-6980, 1994.

Su, W., and A.M. Dziewonski, Simultaneous inversion for 3-D variations in shear and bulk velocity in the mantle, *Phys. Earth Planet. Inter., 100*, 135-156, 1997.

Thurber, C.H. and N. Rabinowitz, (Eds.), *Advances in Seismic Event Location*, Kluwer Acad., Netherlands, pp. 266, 2000.

Trampert, J., and J. Woodhouse, Global phase velocity maps of Love and Rayleigh waves between 40 and 150 seconds, *Geophys. J. Int.*, *122*, 675-690, 1995.

Trampert, J., Vacher, P., and Vlaar, N., Sensitivities of seismic velocities to temperature, pressure, and composition of the lower mantle, *Phys. Earth Planet. Inter., 124*, 255-267, 2001.

van der Hilst, R.D., S. Widiyantoro, and E.R. Engdahl, Evidence for deep mantle circulation from global tomography, *Nature, 386*, 578-584, 1997.

van Wijk, J.W., Govers, R., and K.P. Furlong, Three-dimensional thermal modeling of the California upper mantle: a slab window vs. stalled slab, *Earth Planet. Sci. Lett., 186*, 175-186, 2001.

Villaseñor, A., M.H. Ritzwoller, A.L. Levshin, M.P. Barmin, E.R. Engdahl, W. Spakman, and J. Trampert, Shear velocity structure of Central Eurasia from inversion of surface wave velocities, *Phys. Earth Planet. Inter., 123*, 169 - 184, 2001.

Villaseñor, A., M.P. Barmin, M.H. Ritzwoller, and A.L. Levshin, Computation of regional travel times and station corrections from three-dimensional velocity models, *Stud. Geophys. Geod.,* in press, 2002.

Wessel, P., and W.H.F. Smith, Free software helps map and display data, *Eos Trans. AGU, 72*, 441, 1991.

Wessel, P., and W.H.F. Smith, New version of the Generic Mapping Tools released, *Eos Trans. AGU, 76*, 329, 1995.

Table 1. Cluster parameters for three categories of events: (1) explosions, (2) GT5 earthquakes, (3) GT10 earthquakes.

Cluster No.	Lat[a]	Lon[a]	Depth[a]	$\Delta t_\circ^b$	nevt[c]	nref[d]	GTx[e]	Name
1	47.875	48.139	0.1	0.53	7	7	GT1	Azgir
2	49.954	78.871	0.0	0.81	100	100	GT1-2	Balapan
3	49.784	78.072	0.0	0.66	151	146	GT1-2	Degelen
4	41.580	88.605	0.0	0.43	20	13	GT1-2	Lop Nor
5	73.350	54.820	0.0	-1.65	29	28	GT1-2	Novaya
6	24.049	5.040	0.0	-0.08	5	5	GT0	Sahara
7	36.938	35.825	33.6	-2.89	24	4	GT5	Adana
8	23.486	70.265	19.6	0.36	107	6	GT5	Bhuj
9	30.590	79.124	12.1	-0.18	86	8	GT5	Chamoli
10	40.798	31.219	9.1	-0.64	41	2	GT5	Duzce
11	39.588	39.805	6.4	-1.73	9	3	GT5	Erzin
12	38.822	70.560	7.5	-1.55	28	4	GT5	Garm
13	35.235	-3.930	6.2	-0.91	38	3	GT5	Hoceima
14	40.740	30.223	10.4	-0.51	34	5	GT5	Izmit
15	17.236	73.748	8.2	-0.29	31	10	GT5	Koyna
16	42.475	43.737	7.0	-1.28	35	5	GT5	Racha
17	57.092	122.276	31.5	-1.53	8	3	GT5	Siberia
18	13.513	51.069	10.0	-0.45	55	5	GT10	Aden
19	28.754	34.608	14.0	-1.94	36	1	GT10	Aqaba
20	27.482	33.864	12.8	-1.49	27	1	GT10	Gubal
21	39.660	76.988	19.6	-2.75	72	1	GT10	Jiashi
22	40.957	44.215	5.6	-1.60	11	2	GT10	Spitak
23	33.479	57.111	14.6	-1.95	35	2	GT10	Tabas
Explosions					312	299		
GT5 Earthquakes					441	53		
GT10 Earthquakes					236	12		
Total					989	314		

[a] Hypocentroid location, depth in km.

[b] Cluster time baseline shift appled to teleseismic and regional data, in sec.

[c] Number of GT events in the cluster.

[d] Number of reference events in the cluster.

[e] 95% confidence in location accuracy better than x km.

Table 2. Number of travel times in the groomed arrival time and the empirical phase path anomly data sets.

	Groomed Arrival Times		Empirical Path Anomalies	
	P_n	P	P_n	P
Explosions	1521	477	121	35
GT5	8974	1380	558	108
GT10	3106	539	157	35
total	13601	2396	836	178

Table 3. Fit to empirical phase path anomalies for explosions.

		CUB2.0_TH			AK135	
Cluster No.	Name	RMS[a]	Correl[b]	$\Delta t_\circ$[c]	RMS[a]	$\Delta t_\circ$[c]
1	Azgir	0.96	0.87	1.17	2.63	2.52
2	Balapan	0.99	0.74	1.69	1.33	2.06
3	Degelen	0.99	0.67	0.54	1.09	1.47
4	Lop Nor	1.50	0.62	1.66	1.85	1.25
5	Novaya	0.73	0.82	0.15	1.59	3.14
	average[d]	1.04	0.75	1.04	1.70	2.09

[a] Rms-misfit between observed and predicted travel times, in sec.

[b] Correlation between observed and predicted travel times.

[c] Cluster time baseline shift applied to regional data alone, in sec.

[d] Average of absolute values of cluster values.

Table 4. Fit to empirical phase path anomalies for GT5 earthquakes. Terminology similar to Table 3.

		CUB2.0_TH			AK135	
Cluster No.	Name	RMS	Correl	$\Delta t_\circ$	RMS	$\Delta t_\circ$
7	Adana	1.07	0.50	-1.76	1.18	-2.74
8	Bhuj	1.37	0.76	-0.78	2.00	0.98
9	Chamoli	2.10	0.65	-0.49	2.36	-0.90
10	Duzce	1.32	0.52	-0.14	1.38	-0.90
11	Erzin	1.22	0.77	-1.78	2.14	-2.91
12	Garm	1.17	0.86	-0.89	2.56	-1.71
13	Hoceima	0.76	0.43	-0.67	0.80	-0.33
14	Izmit	1.04	0.57	-0.10	1.14	-0.83
15	Koyna	1.02	0.85	-0.94	1.62	2.31
16	Racha	1.39	0.71	-0.15	1.89	-1.25
17	Siberia	1.13	0.69	-0.65	1.55	-0.98
	average	1.24	0.67	0.76	1.70	1.44

Table 5. Fit to empirical phase path anomalies for GT10 earthquakes. Terminology similar to Table 3.

		CUB2.0_TH			AK135	
Cluster No.	Name	RMS	Correl	$\Delta t_\circ$	RMS	$\Delta t_\circ$
19	Aqaba	1.60	0.31	-0.11	1.54	-0.74
20	Gubal	1.02	0.76	0.09	1.78	-0.98
21	Jiashi	2.07	0.77	0.40	2.99	-1.57
22	Spitak	1.24	0.84	-0.08	2.28	-1.45
23	Tabas	1.74	0.37	-0.71	1.88	-2.42
	average	1.54	0.61	0.28	2.10	1.43

Table 6. Location results for nuclear explosions.

				CUB2.0_TH		AK135	
Cluster No.	Name	Events[a]	Stations[b]	Error[c]	RMS[d]	Error[c]	RMS[d]
1	Azgir	6	19	4.2	1.08	24.0	1.49
2	Balapan	10	25	3.9	1.10	11.2	1.22
3	Degelen	3	18	3.1	1.01	12.0	1.36
4	Lop Nor	16	45	6.1	1.22	9.6	1.49
5	Novaya	3	15	8.0	1.03	13.6	1.57
	overall[e]	38	24	5.1	1.09	14.1	1.43

[a] Number of events with open azimuth $< 180^\circ$ and ≥ 5 stations.

[b] Median number of stations.

[c] Average distance from estimated to GT location, in km.

[d] Rms difference between observed and predicted travel times, in sec.

[e] Total or average of cluster values.

Table 7. Location results for GT5 earthquakes. Terminology similar to Table 6.

				CUB2.0_TH		AK135	
Cluster No.	Name	Events	Stations	Error	RMS	Error	RMS
7	Adana	19	23	8.8	1.04	8.1	1.17
8	Bhuj	4	15	11.5	1.00	8.5	1.42
9	Chamoli	50	17	10.8	1.20	20.8	1.54
10	Duzce	21	45	7.3	1.23	6.6	1.33
11	Erzin	8	33	6.0	1.29	9.5	1.61
12	Garm	26	21	5.2	1.12	9.7	2.17
13	Hoceima	21	26	4.4	0.90	7.5	0.86
14	Izmit	8	116	5.1	1.07	5.3	1.10
15	Koyna	8	10	5.5	1.13	10.7	1.23
16	Racha	34	20	8.2	1.15	21.8	1.43
17	Siberia	8	33	6.3	1.13	11.0	1.31
	overall	207	32	7.2	1.12	10.9	1.38

Table 8. Location results for GT10 earthquakes. Terminology similar to Table 6.

				CUB2.0_TH		AK135	
Cluster No.	Name	Events	Stations	Error	RMS	Error	RMS
19	Aqaba	14	47	17.6	1.17	13.8	1.27
20	Gubal	10	16	9.8	1.12	14.9	1.31
21	Jiashi	61	12	16.6	0.87	20.0	1.69
22	Spitak	10	32	8.3	1.24	9.1	1.69
23	Tabas	26	19	9.3	1.17	8.7	1.27
	overall	121	25	12.3	1.11	13.3	1.44

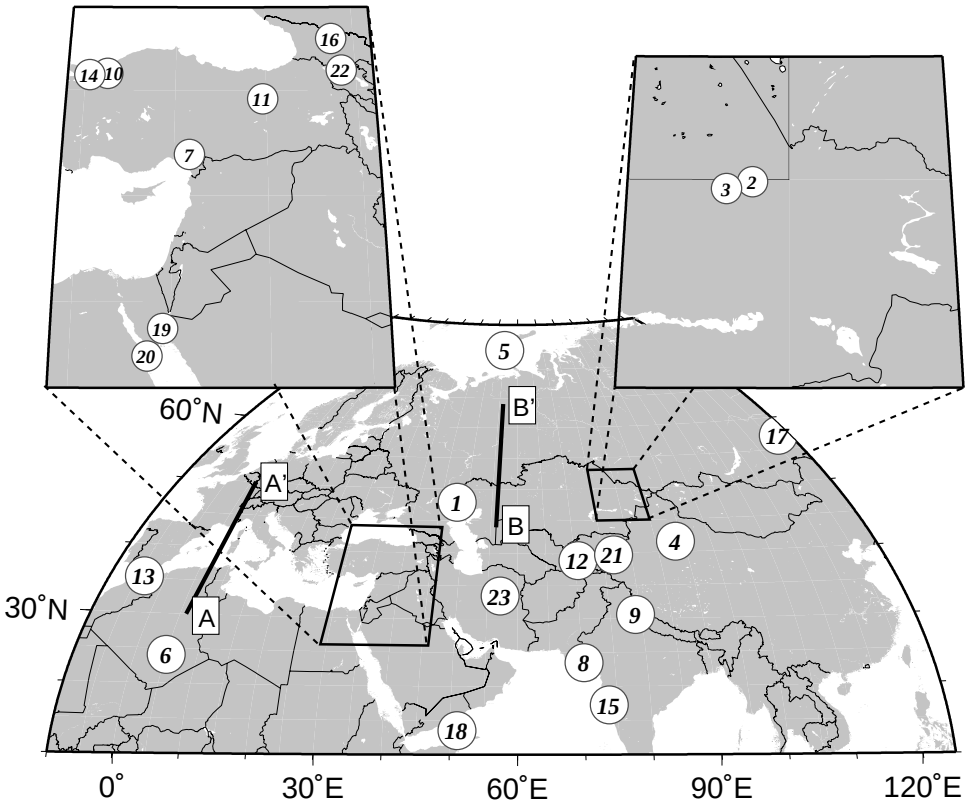

Figure 1. Locations of the explosion and earthquake clusters. Numbers refer to clusters identified in Table 1. Lines $A - A'$ and $B - B'$ refer to the vertical model profiles shown in Figure 8.

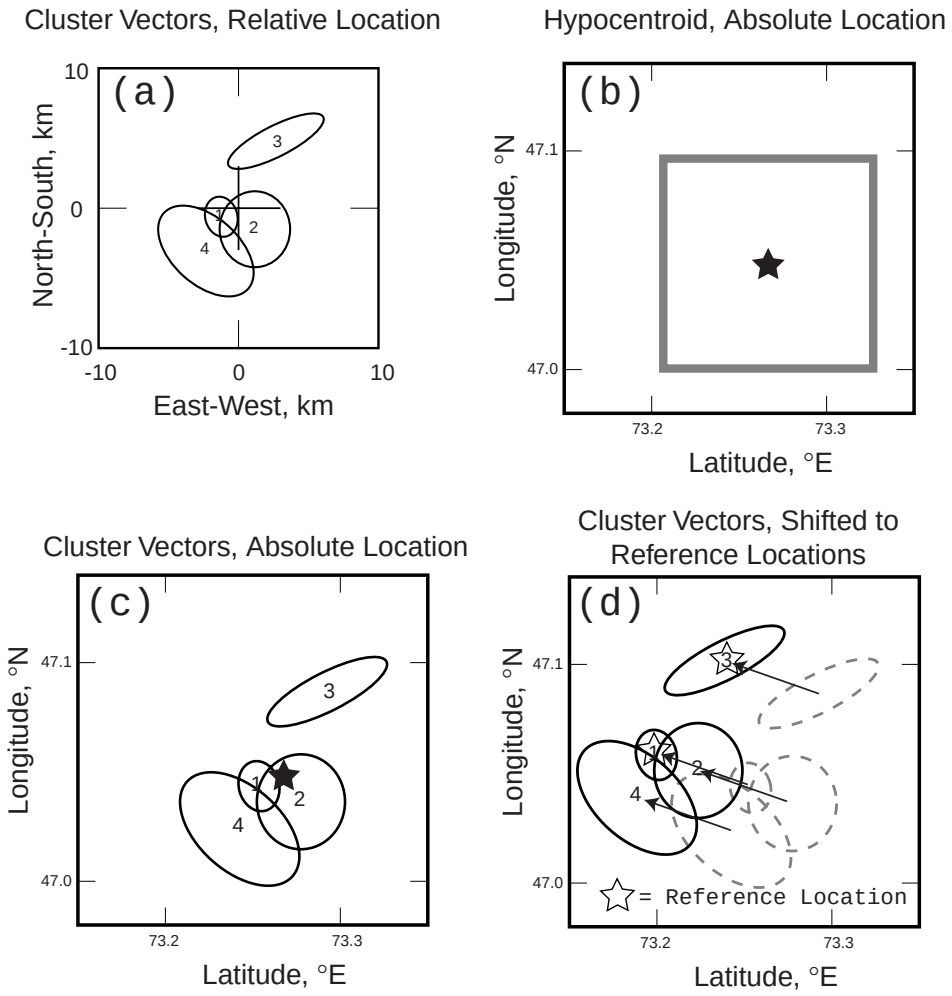

Figure 2. Schematic of the HDC analysis used to generate the GT data base in this study. (a) Relative locations of cluster event epicenters ("cluster vectors") are shown with 90% confidence ellipses. Locations are relative to the hypocentroid, the geometric mean of current absolute locations of all events. (b) The hypocentroid (solid star) is located using all cluster event arrival time data (appropriately shifted) as if it were an earthquake, using the 1-D model AK135. The box corresponds to (a). (c) The relative locations from (a) are added to the absolute location of the hypocentroid in (b) to give absolute locations for all events in the cluster, with confidence ellipses scaled from (a). (d) Finally, the location bias is removed by shifting the cluster to match the reference event locations (from independent local seismic data) that have been obtained for this cluster. Reference locations for event 1 and 3 are shown by open stars. All cluster events are shifted by the same vector, the average of the shifts calculated from the reference locations and the corresponding HDC locations in (c). The shifted locations for all cluster events in (d) compose the GT location data base.

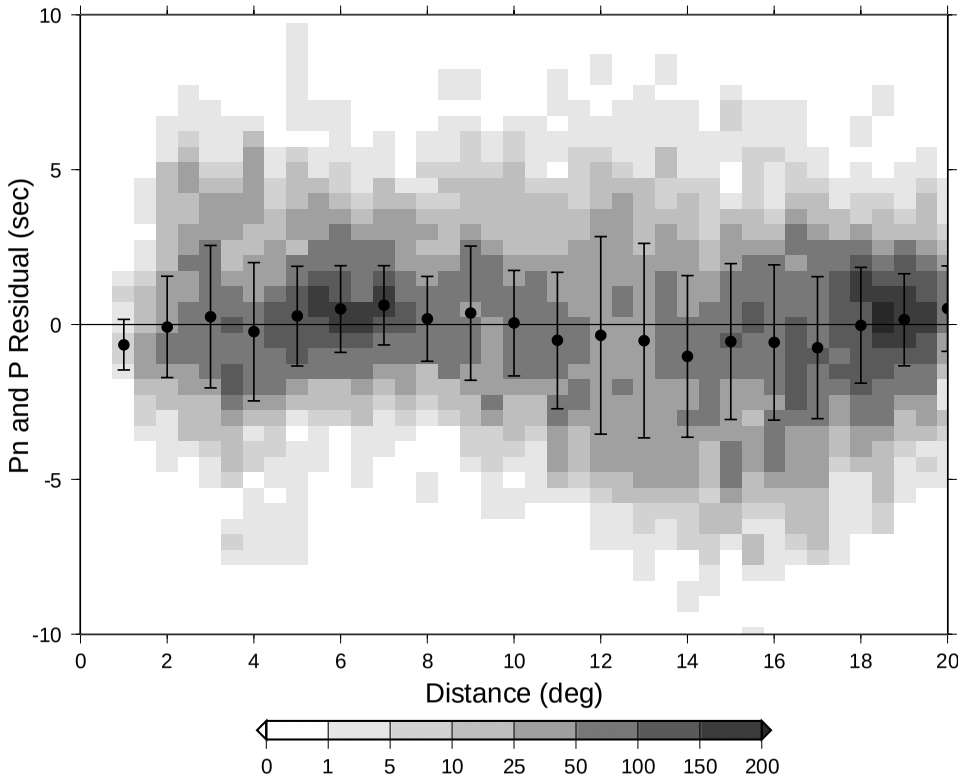

Figure 3. Residual density plot for P_n and P phases in the groomed arrival time data set. Residuals are taken with respect to AK135 travel times. Station cluster residuals corrected for the cluster event static are binned at 0.5 degrees in distance and 0.5 sec in time. Bin hit counts are plotted according to the scale. Estimates of the residual median and spread at one-degree intervals are also plotted as circles and vertical lines, respectively.

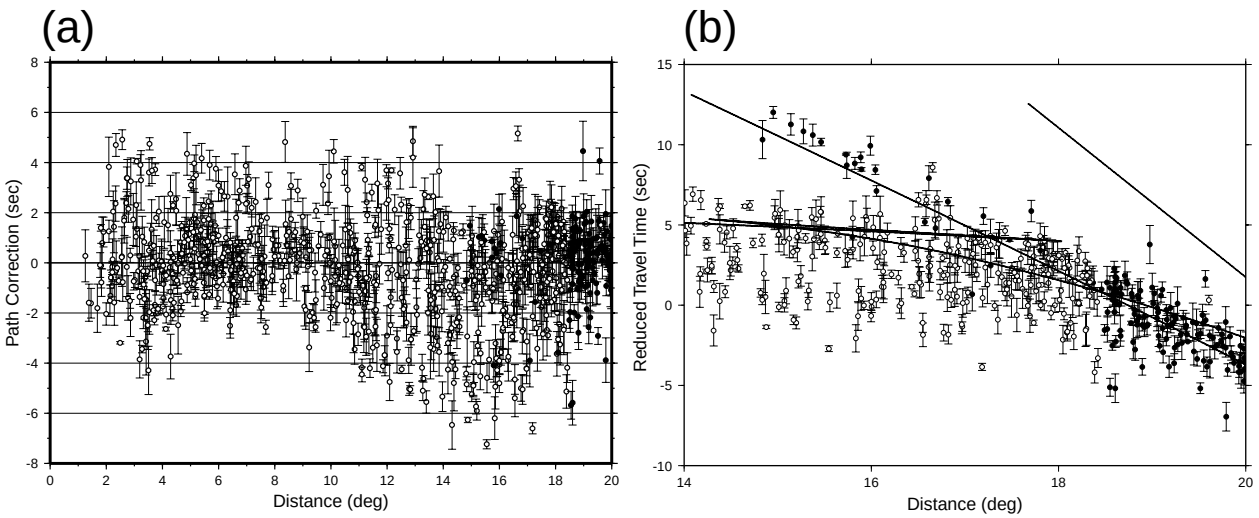

Figure 4. Reduced P_n (white) and P (black) empirical phase path anomalies plotted as the median and spread estimates with respect to distance. Travel times are corrected for cluster time baseline shifts. (a) Results are presented as residuals with respect to the AK135 travel times. (b) Results are presented near the P_n/P cross-over as reduced travel times (relative to 8.0 km/s). AK135 predicted P_n and P travel time branches are also shown.

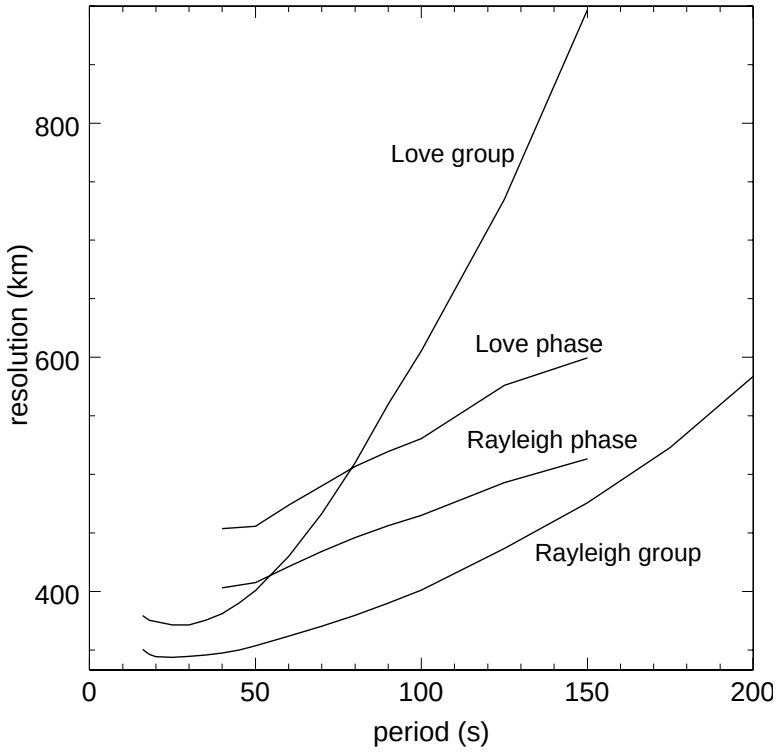

Figure 5. Resolution of the dispersion maps averaged across the region of study (Figure 1).

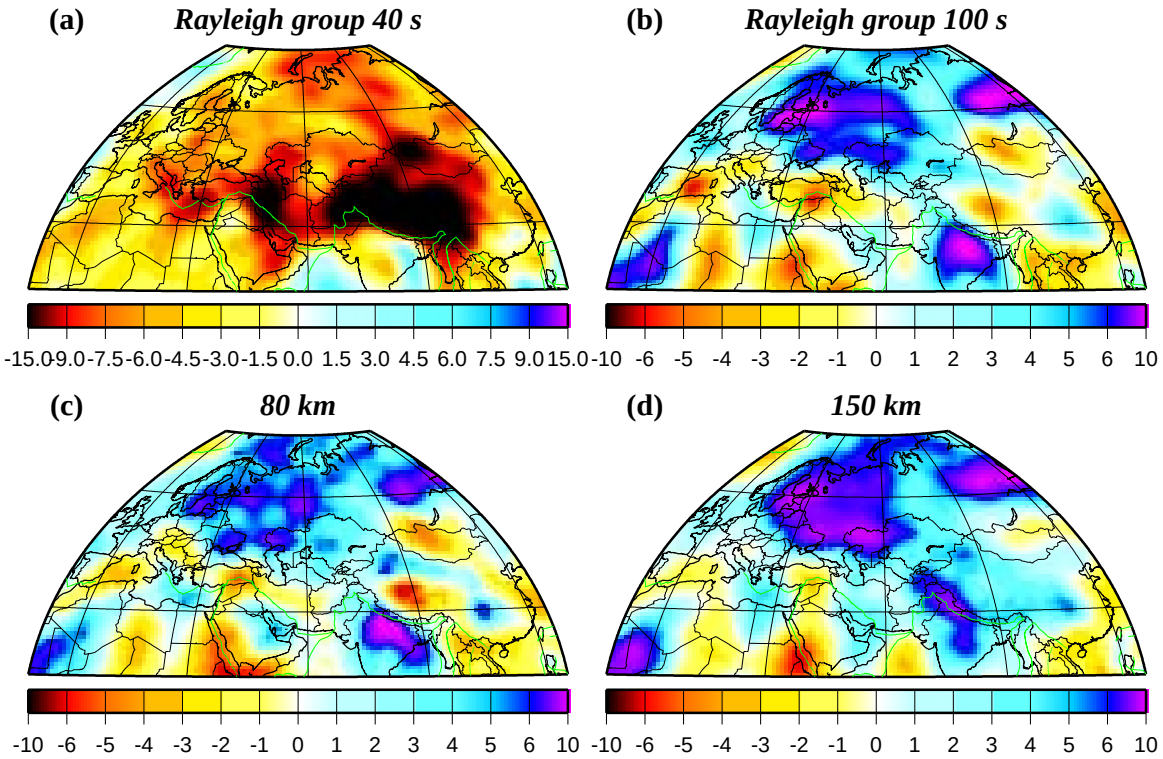

Figure 6. Dispersion maps and horizontal slices of the model at the periods and depths indicated.

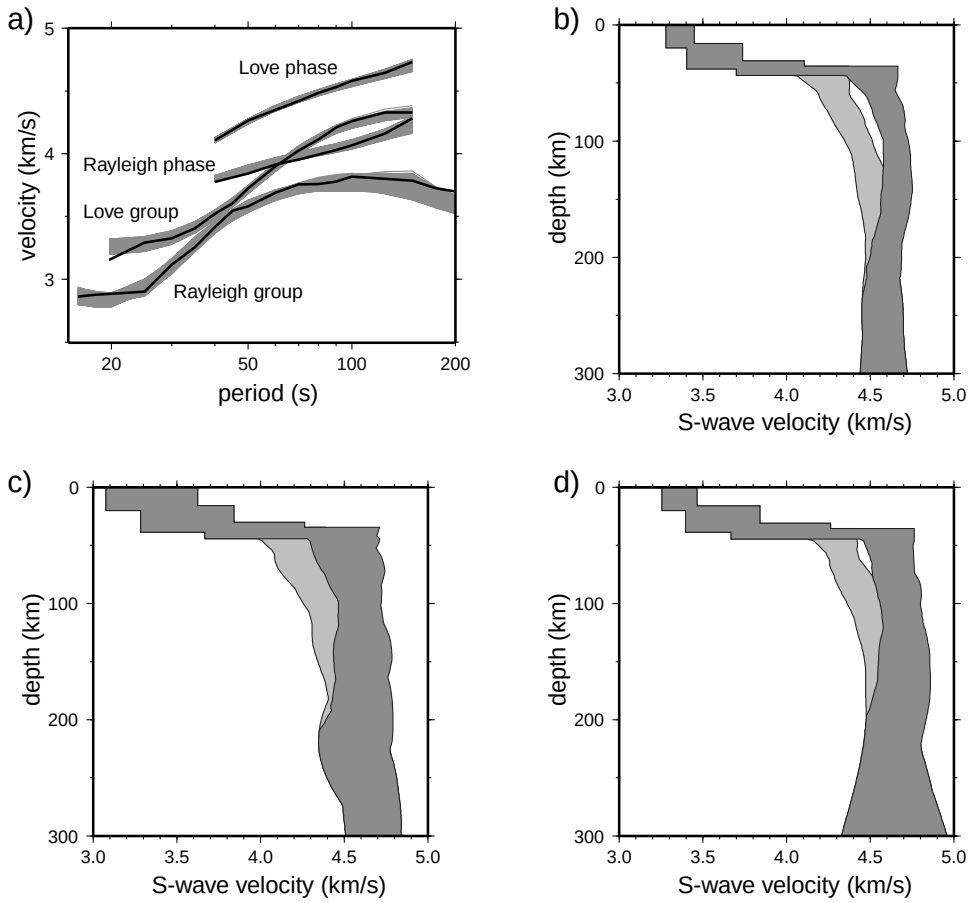

Figure 7. (a) Observed dispersion curves at a point in Iran (30°N, 60°E). The black lines are observations derived from the dispersion maps and the grey shaded zones represent the range of dispersion curves from the the ensemble of acceptable models shown in (b). Inversion results for three data sets: (b) simultaneous inversion of group and phase speeds (CUB2.0), (c) group speed alone, and (d) phase speed alone. The full width of the ensemble of acceptable models is indicated, where v_{sh} is dark grey and v_{sv} is light grey.

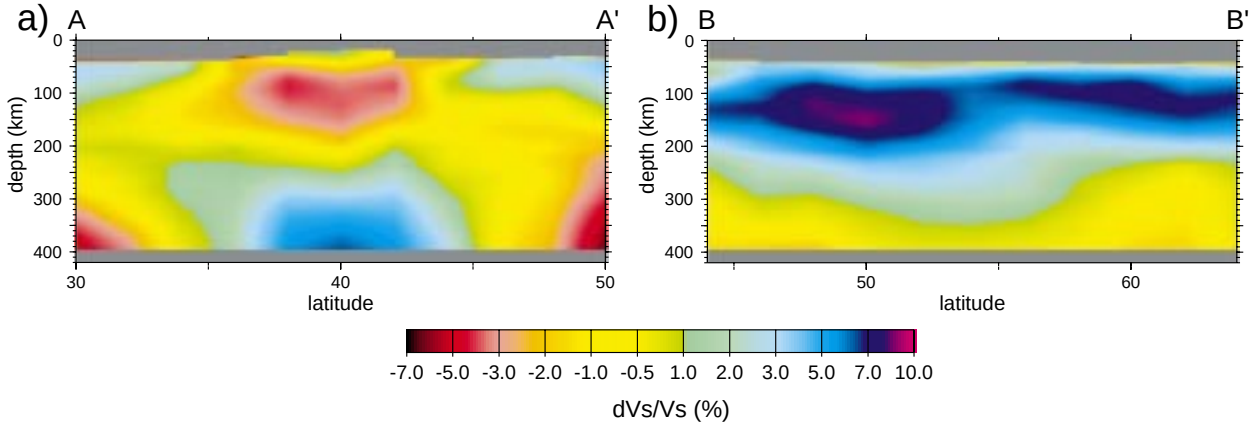

Figure 8. Vertical slices of the v_s model from CUB2.0 plotted as percent deviation from AK135. Locations of the profiles are shown in Figure 1.

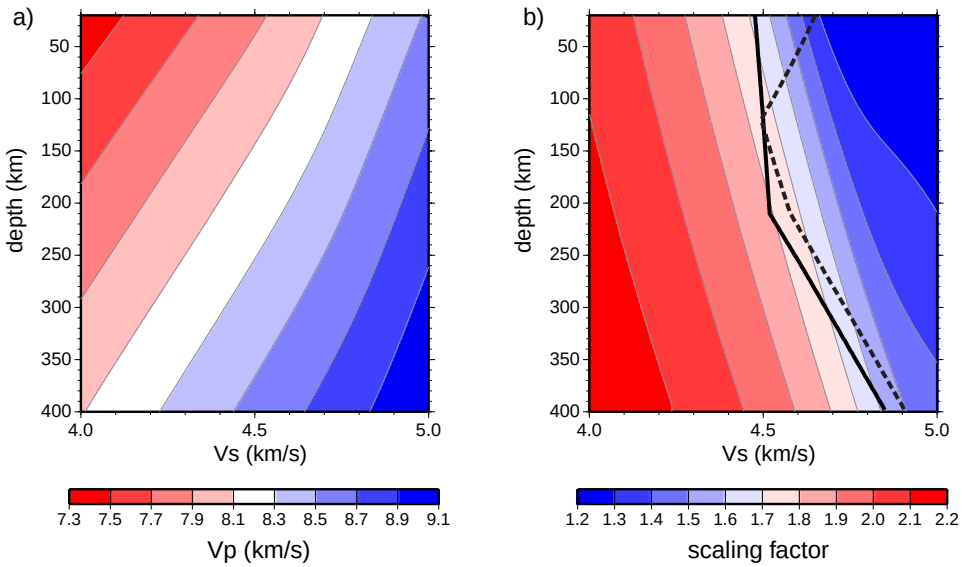

Figure 9. (a) Grid used for the theoretical v_s to v_p conversion. (b) The theoretical conversion presented as the logarithmic scaling factor $d \ln v_s / d \ln v_p$. The solid black line is v_s from the 1-D model AK135 and the dashed line is v_s converted from AK135 v_p by the theoretical conversion.

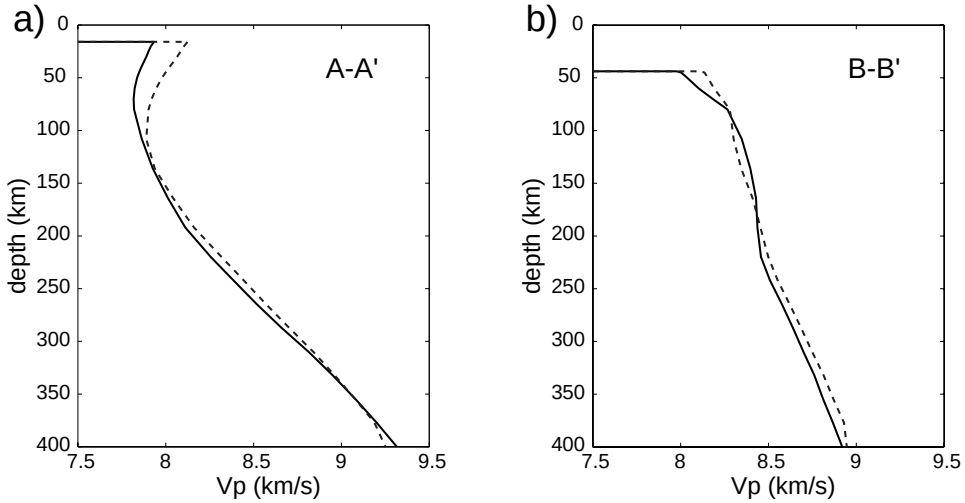

Figure 10. v_p model at the mid-points of profiles (a) $A-A'$ and (b) $B-B'$ from Figures 1 and 8a. The solid line represents the theoretical conversion from v_s (i.e., CUB2.0_TH) and the dashed line is from the empirical scaling relation $d\ln v_s/d\ln v_p = 2.0$ in which AK135 is used as the reference (i.e., CUB2.0_EMP).

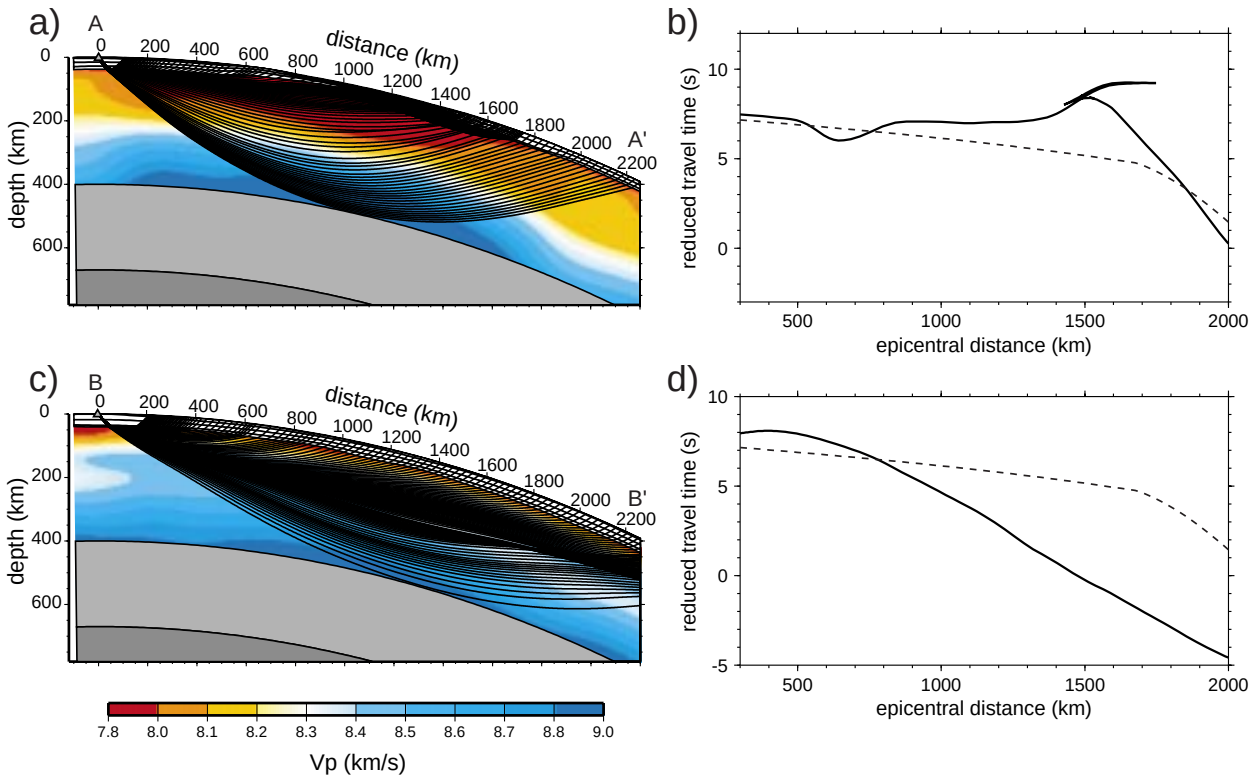

Figure 11. (a) and (b) P_n rays traced through the vertical slices of CUB2.0_TH from Figure 1 and 8. P-velocities in the upper mantle underlie the rays. (c) and (d) The reduced P_n travel time curves for each slice (relative to 8.0 km/s), shown as solid lines, are compared with the P_n first arrivals for AK135. This demonstrates the complexity of P_n.

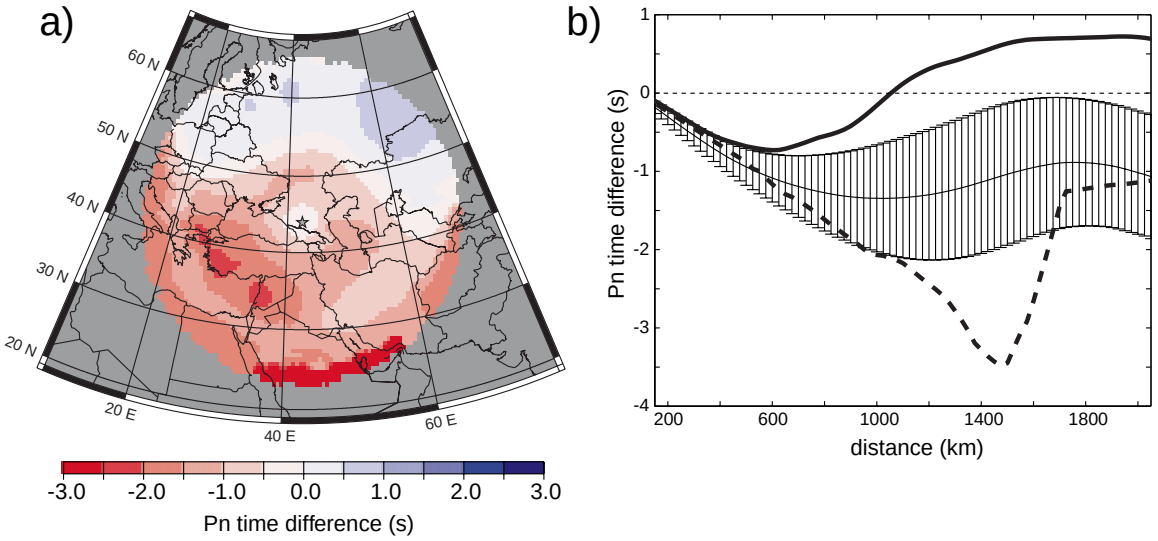

Figure 12. Effect of the v_s to v_p conversion on P_n travel times. (a) Difference between P_n travel times from CUB2.0_TH and CUB2.0_EMP centered on stations KIV (Kislovodsk, Russia). Positive values mean CUB2.0_TH travel times are faster than those from CUB2.0_EMP. (b) Solid line shows the P_n travel time difference for profile $B - B'$ and the dashed line for $A - A'$ from Figures 1 and 8. One standard deviation errors bars show the geographical average across the region of study (Figure 1).

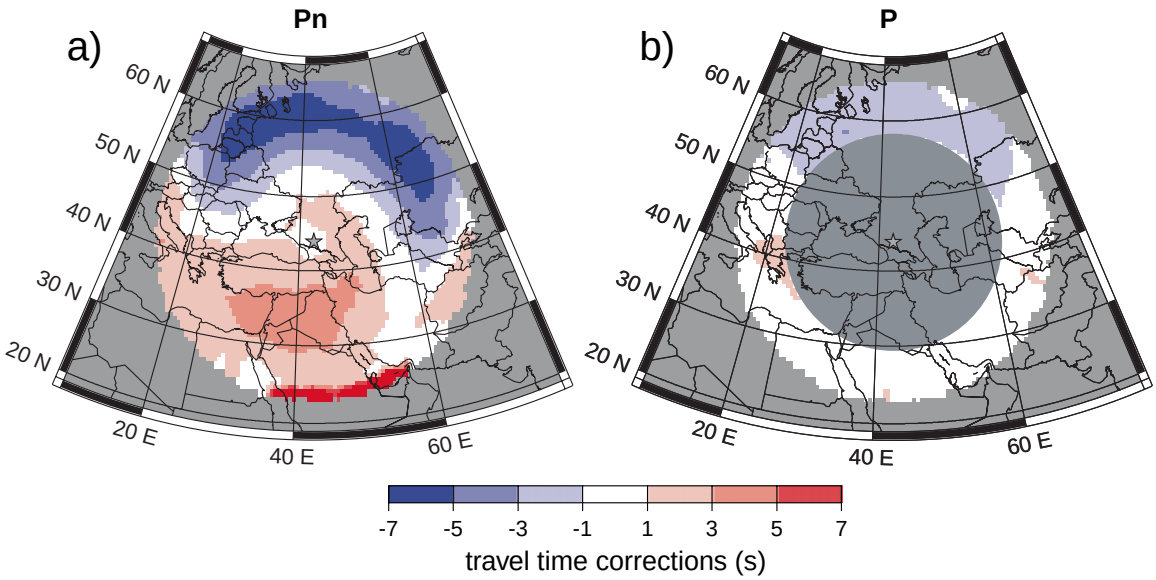

Figure 13. Example of P_n and P travel time correction surfaces computed for a surface source for station KIV. The corrections here are relative to the 1-D model IASP91 [*Kennett & Engdahl*, 1991].

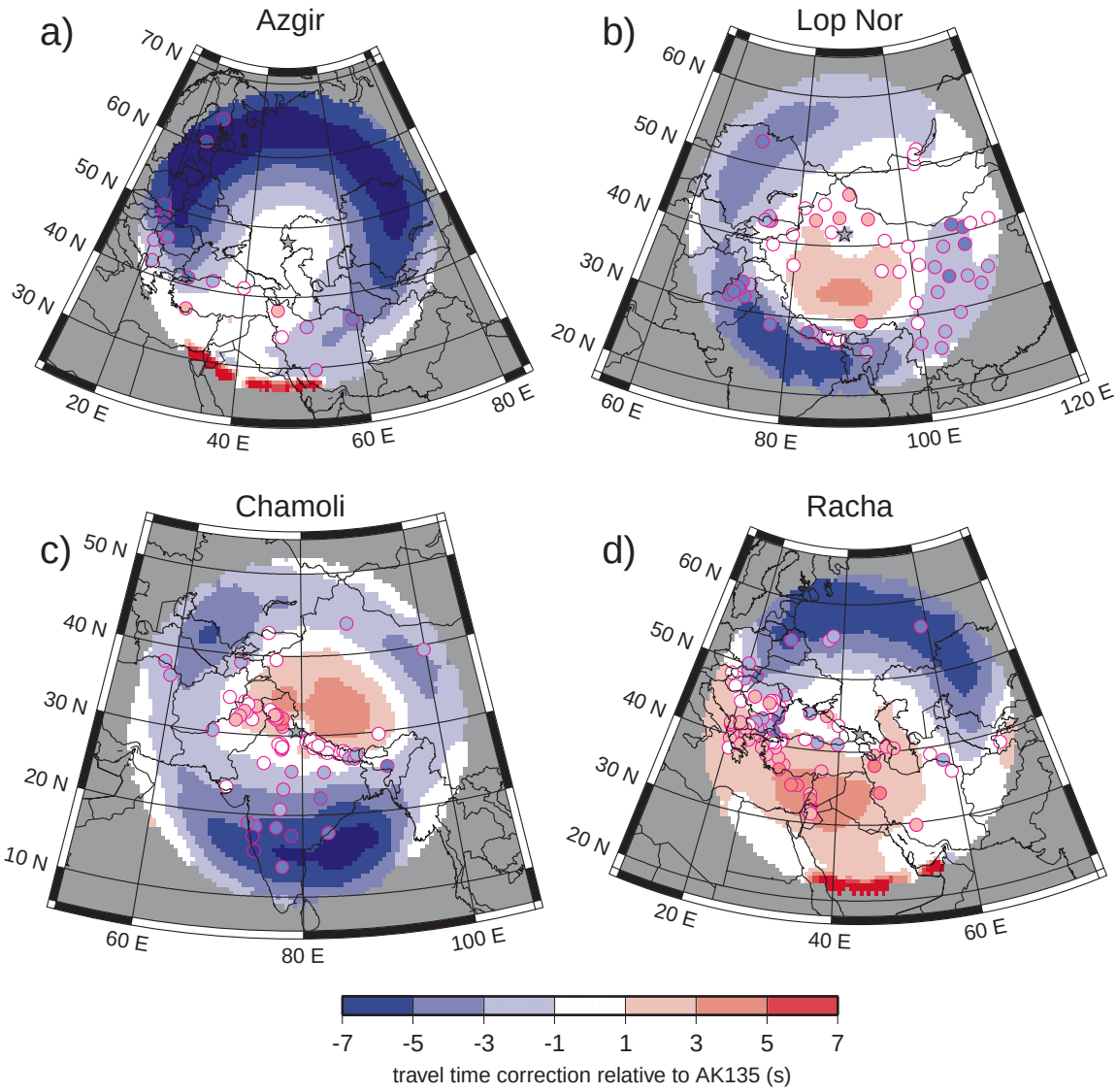

Figure 14. Cluster-centered travel time correction surfaces for four cluster regions. The colored contours are the predictions from the 3-D model CUB2.0_TH referenced to the travel time from the 1-D model AK135. The symbols are the empirical phase path anomalies, color-coded similarly to the model predictions. The cluster time baseline shift is indicated in Tables 3 and 4. (a) and (b) are explosions in the Azgir and Lop Nor clusters and (c) and (d) are earthquakes in the Chamoli and Racha clusters, respectively.

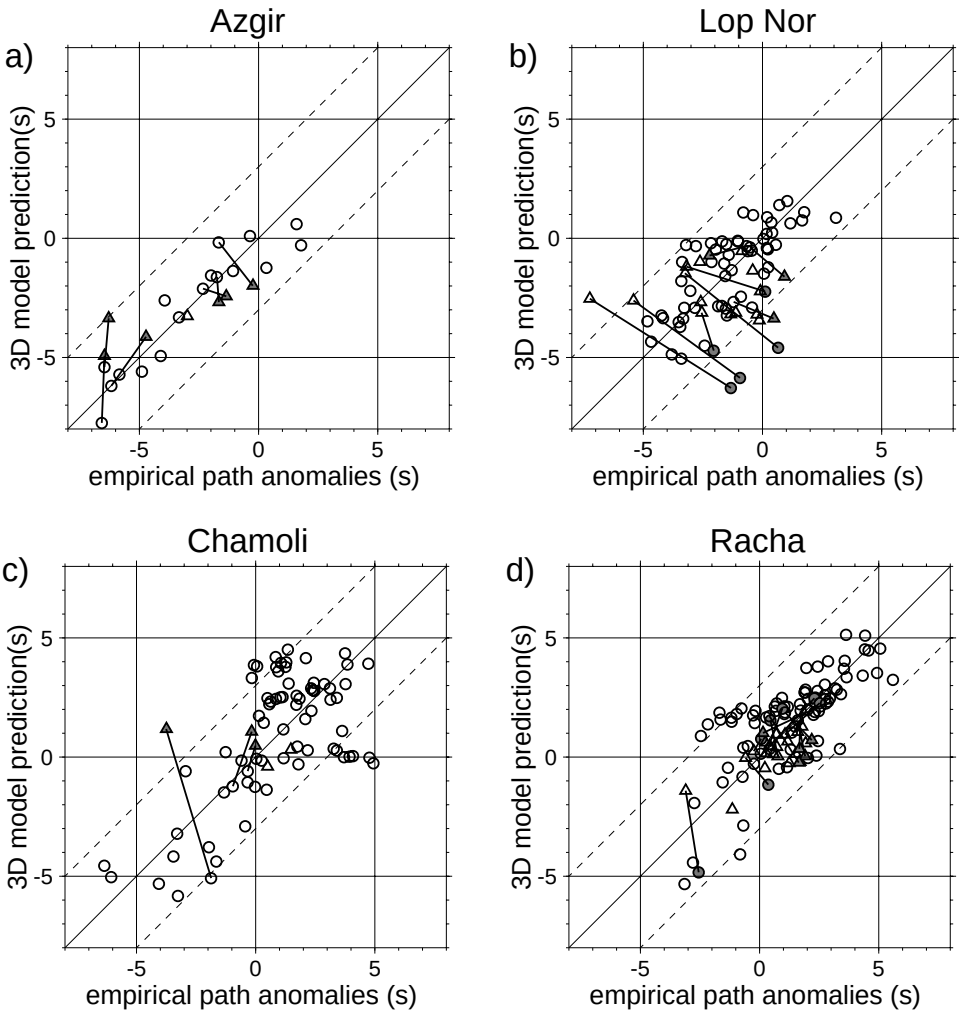

Figure 15. Comparison between the P and P_n travel times predicted by the 3-D model CUB2.0_TH and the empirical phase path anomalies for the four event clusters shown in Figure 14. The empirical path anomalies are on the horizontal axis, paired with the model predictions on the vertical axis. Circles are P_n and triangles are P. Phases have been re-identified using the 3-D model; bars link phases originally identified with the 1-D model AK135 (shaded gray) to the re-identified phases (unshaded). The cluster time baseline shifts listed in Tables 3 and 4 have been applied. The dashed lines mark the location of ± 3 sec residuals.

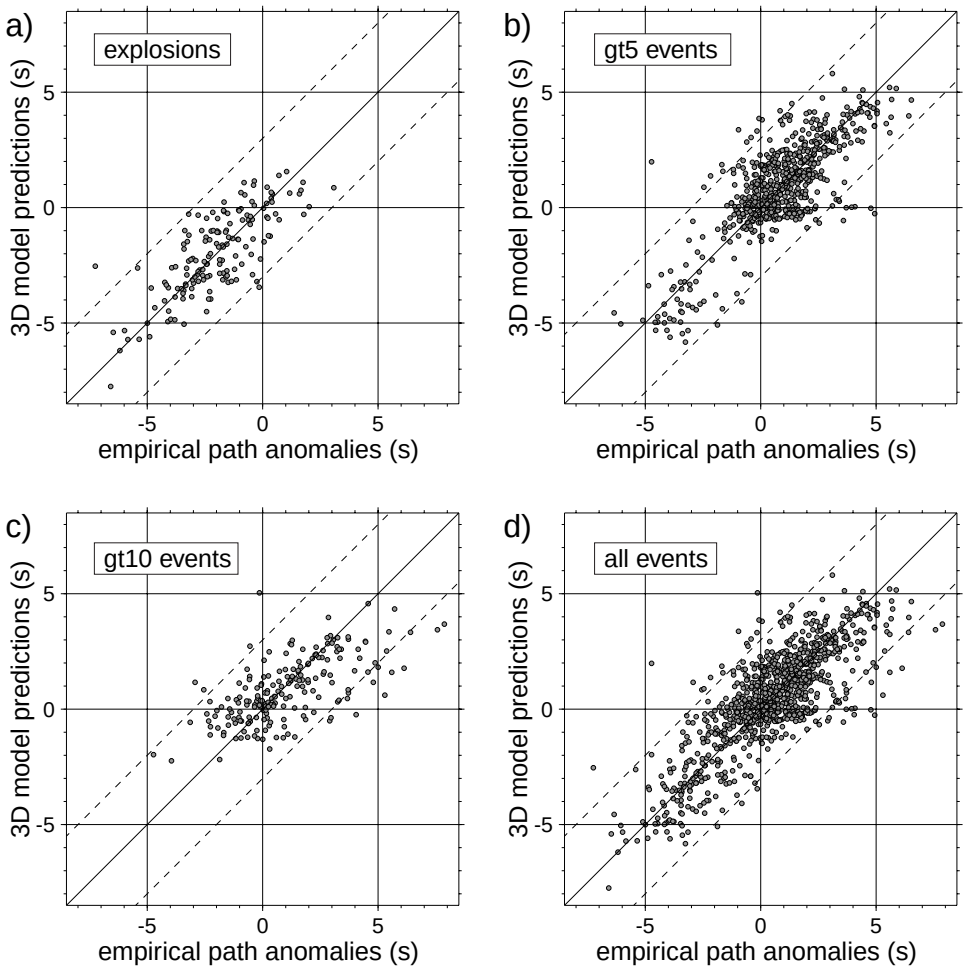

Figure 16. Overall comparison between the P and P_n travel times predicted by the 3-D model CUB2.0_TH and the empirical phase path anomalies. Similar to Figure 15. The cluster time baseline shifts listed in Tables 3 - 5 have been applied and misfit statistics are also listed in these tables.

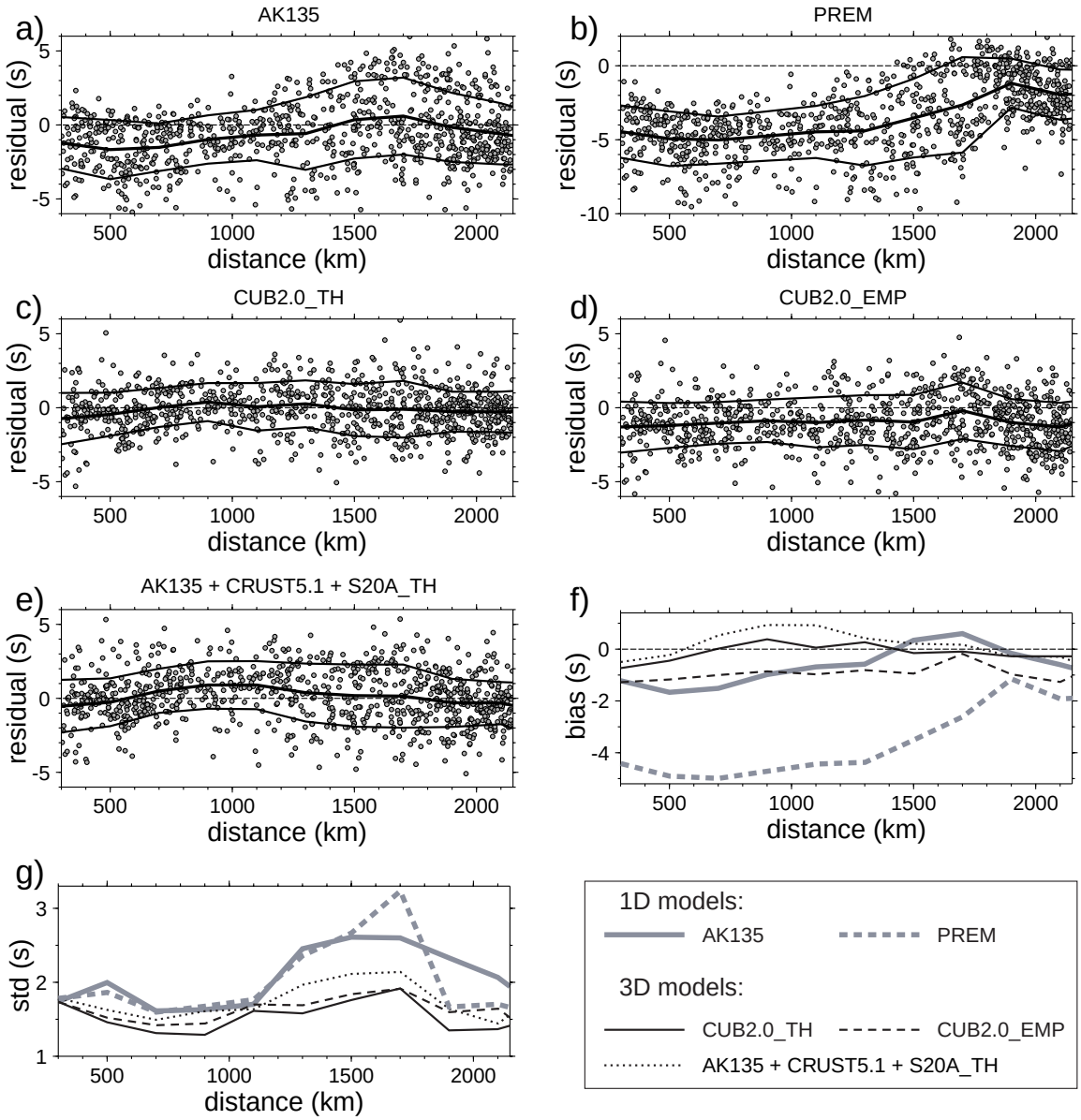

Figure 17. (a) - (e) Residual between the empirical phase path anomalies for P_n and P and predictions from a number of models, plotted versus epicentral distance. Running average (bias) and standard deviation are shown as the black lines. Cluster time baseline shifts have not been applied. (f) - (g) The running residual bias and standard deviation shown for the various models.

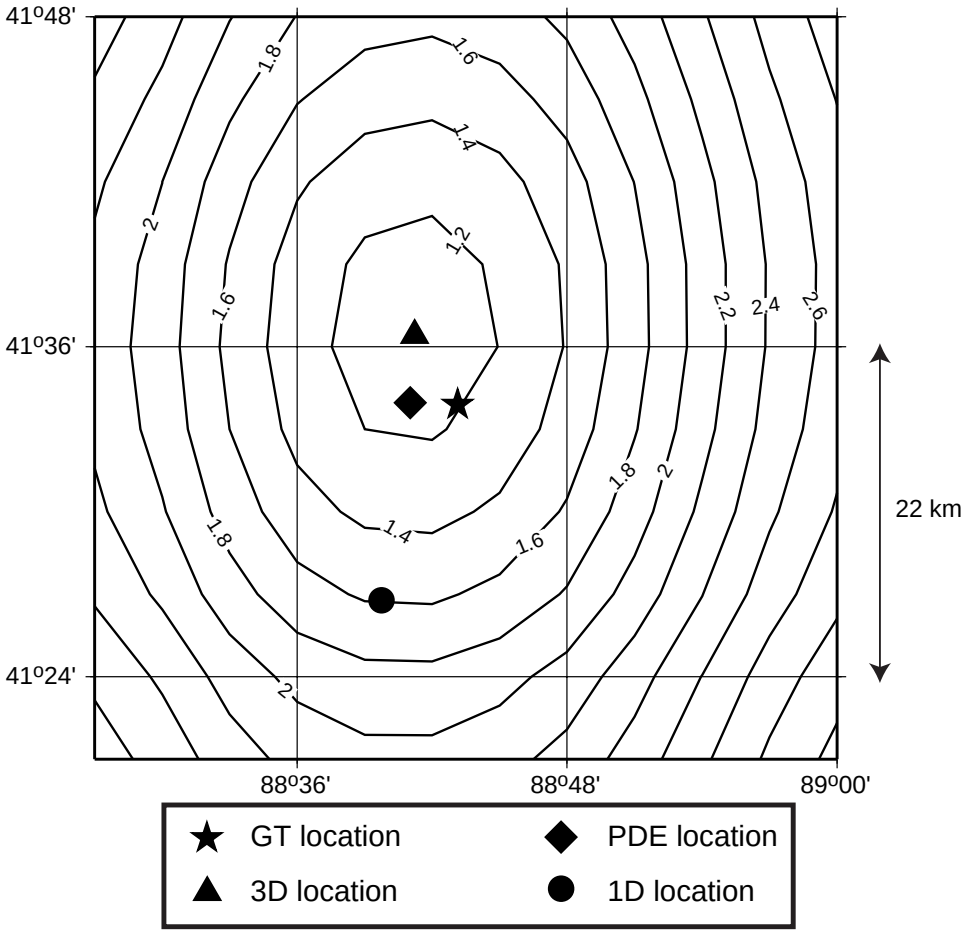

Figure 18. Contours of rms-misfit using the 3-D model CUB2.0_TH for a grid of hypothesized epicenters for an explosion at the Lop Nor test site (May 26, 1990; 54 reporting stations). Units are seconds. The GT1-2 location is indicated with a star, the best-fit locations using the 3-D and 1-D models are shown with a triangle and a circle, respectively, and the PDE location is shown with a diamond.

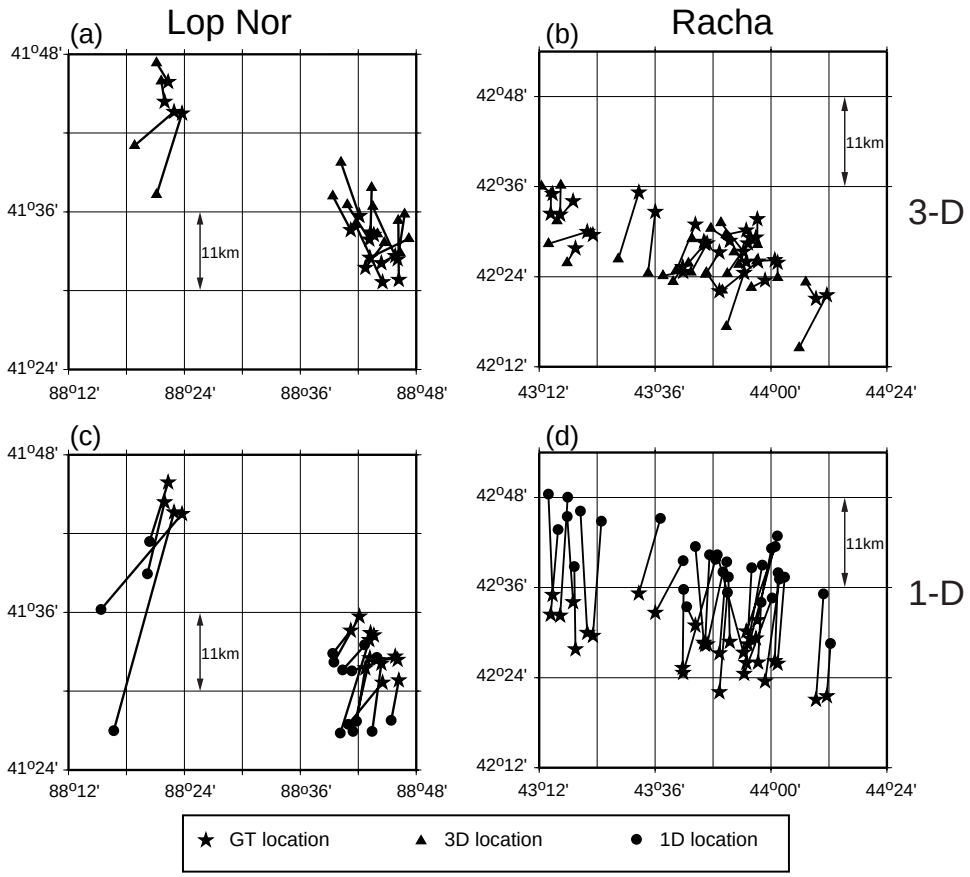

Figure 19. Mislocation vectors from two event clusters for (left column) explosions on the Lop Nor test site and (right column) earthquakes near Racha, Georgia. (a) and (b) 3-D model (CUB2.0_TH) locations. (c) and (d) 1-D model (AK135) locations. Stars mark GT locations, triangles and circles are 3-D and 1-D model locations, respectively.

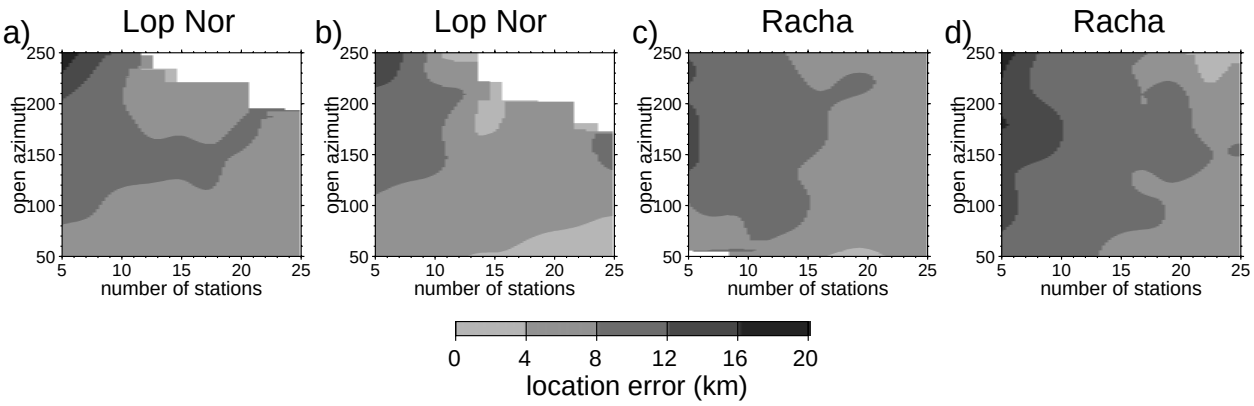

Figure 20. Mislocation using the 3-D model CUB2.0_TH, presented as a function of number of stations and open azimuth, determined by randomly choosing subsets of the reported travel times for four events: (a) Lop Nor, May 26, 1990; (b) Lop Nor, Sept 25, 1992; (c) Racha, May 3, 1991; (d) Racha, July 4, 1991.

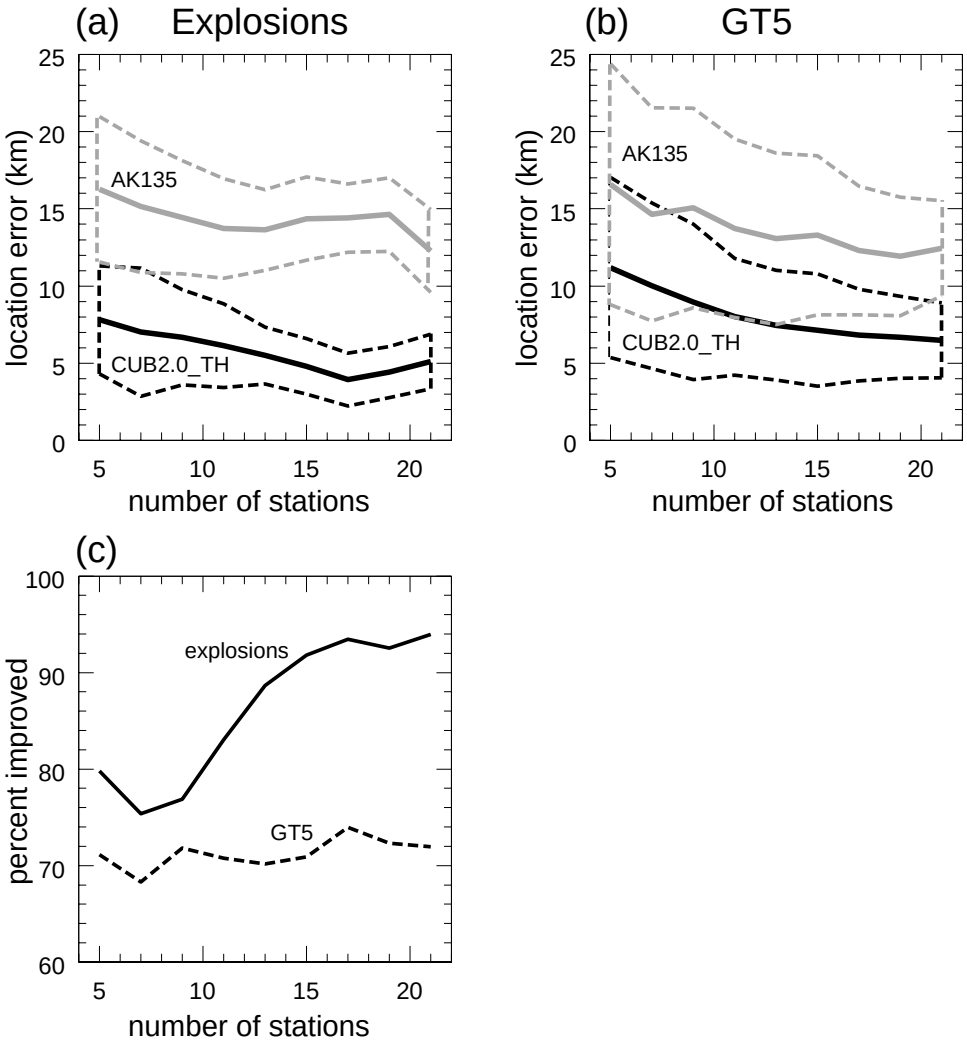

Figure 21. Location error for the 3-D and 1-D models, plotted as a function of the number of reporting stations, determined by randomly choosing subsets of the reported travel times in which open-azimuth is constrained to be less than 180°. (a) and (b) Average (solid lines) and standard deviation (dashed lines) are shown for explosions and GT5 earthquakes for CUB2.0_TH (black lines) and AK135 (grey lines). (c) Percent of the events for which the location error is smaller using the 3-D model than the 1-D model for explosions (solid line) and GT5 earthquakes (dashed line).